

# ST3GAL1 and $\beta$ II-spectrin pathways control CAR T cell migration to target tumors

Received: 16 June 2022

Accepted: 21 March 2023

Published online: 17 April 2023

 Check for updates

Yeonsun Hong<sup>1,11</sup>, Brandon L. Walling<sup>1,11</sup>, Hye-Ran Kim<sup>1</sup>, William S. Serratelli<sup>1</sup>, John R. Lozada<sup>1</sup>, Cooper J. Sailer<sup>1,2</sup>, Andrea M. Amitrano  <sup>1,2</sup>, Kihong Lim  <sup>1</sup>, Raj Kumar Mongre<sup>1</sup>, Kyun-Do Kim<sup>3</sup>, Tara Capece<sup>1</sup>, Elena B. Lomakina<sup>4</sup>, Nicholas S. Reilly<sup>5</sup>, Kevin Vo<sup>1</sup>, Scott A. Gerber<sup>6</sup>, Tan-Chi Fan<sup>7</sup>, Alice Lin-Tsing Yu<sup>8</sup>, Patrick W. Oakes<sup>5</sup>, Richard E. Waugh  <sup>4</sup>, Chang-Duk Jun  <sup>9</sup>, Patrick M. Reagan<sup>10</sup> & Minsoo Kim  

Adoptive transfer of genetically engineered chimeric antigen receptor (CAR) T cells is becoming a promising treatment option for hematological malignancies. However, T cell immunotherapies have mostly failed in individuals with solid tumors. Here, with a CRISPR–Cas9 pooled library, we performed an *in vivo* targeted loss-of-function screen and identified ST3  $\beta$ -galactoside  $\alpha$ -2,3-sialyltransferase 1 (ST3GAL1) as a negative regulator of the cancer-specific migration of CAR T cells. Analysis of glycosylated proteins revealed that CD18 is a major effector of ST3GAL1 in activated CD8<sup>+</sup> T cells. ST3GAL1-mediated glycosylation induces the spontaneous nonspecific tissue sequestration of T cells by altering lymphocyte function-associated antigen-1 (LFA-1) endocytic recycling. Engineered CAR T cells with enhanced expression of  $\beta$ II-spectrin, a central LFA-1-associated cytoskeleton molecule, reversed ST3GAL1-mediated nonspecific T cell migration and reduced tumor growth in mice by improving tumor-specific homing of CAR T cells. These findings identify the ST3GAL1– $\beta$ II-spectrin axis as a major cell-intrinsic program for cancer-targeting CAR T cell migration and as a promising strategy for effective T cell immunotherapy.

Adoptive transfer of therapeutic T cells is a promising approach with complete and durable responses in several disease conditions, such as viral infection, autoimmune disease, atherosclerosis and cancer<sup>1</sup>. For example, using chimeric antigen receptor (CAR) T cells has proven effective in treating hematological malignancies<sup>2</sup>. However, a major limitation to effective T cell immunotherapy is the physical access of immune cells to the target sites. Even if therapeutic T cells can recognize

and kill target cells, they will fail *in vivo* if they cannot infiltrate into target tissues.

After intravenous transfer into humans, most transferred T cells are detected at non-tumor-bearing tissues, with only a small percentage eventually reaching target tumor sites<sup>3</sup>. This is a clinically important issue, as sequestration of ex vivo generated T cells at nonspecific tissue sites after intravenous transfer is often associated with impaired

<sup>1</sup>Department of Microbiology and Immunology, David H. Smith Center for Vaccine Biology and Immunology, University of Rochester, Rochester, NY, USA.

<sup>2</sup>Department of Pathology, University of Rochester Medical Center, Rochester, NY, USA. <sup>3</sup>Department of Convergent Research of Emerging Virus Infection, Korea Research Institute of Chemical Technology, Daejeon, Korea. <sup>4</sup>Department of Biomedical Engineering, University of Rochester Medical Center, Rochester, NY, USA. <sup>5</sup>Department of Physics and Astronomy, University of Rochester, Rochester, NY, USA. <sup>6</sup>Department of Surgery, University of Rochester, Rochester, NY, USA. <sup>7</sup>Institute of Stem Cell and Translational Cancer Research, Chang Gung Memorial Hospital at Linkou and Chang Gung University, Taoyuan, Taiwan. <sup>8</sup>Department of Pediatrics/Hematology Oncology, University of California in San Diego, San Diego, CA, USA. <sup>9</sup>School of Life Sciences, Gwangju Institute of Science and Technology (GIST), Gwangju, Korea. <sup>10</sup>Wilmot Cancer Institute, University of Rochester Medical Center, Rochester, NY, USA. <sup>11</sup>These authors contributed equally: Yeonsun Hong, Brandon L. Walling.  e-mail: [minsoo\\_kim@urmc.rochester.edu](mailto:minsoo_kim@urmc.rochester.edu)

trafficking of T cells to target tissues<sup>3</sup> and the development of acute toxicity<sup>4</sup>. Owing to the inefficient trafficking of transferred CAR T cells to target tumor sites, clinical success of CART cell immunotherapy has not yet been achieved for many solid tumors<sup>5</sup>. For the same reason, individuals require a large number of highly activated engineered cells delivered intravenously, which further increases both cellular manufacturing costs and the risk of T cell toxicity and systemic cytokine release syndrome (CRS).

The goal of the present study was to understand why in vitro activated CD8<sup>+</sup> T cells can get trapped in off-target tissue sites after being intravenously transferred. Here, we propose that autologous therapeutic T cells undergo molecular and cellular reprogramming during the ex vivo manufacturing process and that the intrinsic changes are important for robust T cell activation and expansion but do not drive T cell migration toward target sites and might increase toxicity. We identified molecular mechanisms that could be harnessed to improve homing of T cells to target sites, thus increasing the efficacy of T cell immunotherapy while reducing the risks associated with nonspecific cytotoxicity<sup>6</sup>.

## Results

### CAR T cells accumulate in the lungs immediately after adoptive transfer

Early clinical studies with CD19 CART cells (CTL019) showed that after T cell infusion, there was an immediate and prolonged decline in circulating CTL019 cells in blood for up to 7 d, which could be directly attributed to nonspecific distributions of CART T cells to random tissue sites<sup>7,8</sup>. Similarly, after treatment with lympho-depleting chemotherapy followed by infusion of  $1 \times 10^8$  to  $2 \times 10^8$  viable CAR<sup>+</sup> T cells (Fig. 1a), all individuals had undetectable circulating T cells for more than 2 d, and significant T cell expansions did not occur until day 14 (Fig. 1b).

To further investigate the spatial and temporal fates of intravenously infused CART T cells in vivo, mouse CD8<sup>+</sup> T cells were retrovirally transduced with trastuzumab (4D5; anti-HER2)-based CAR<sup>9</sup> at >92% efficiency (Extended Data Fig. 1a). Co-incubation of the B16 mouse melanoma cell line that stably expresses human HER2 antigen (B16-hHER2; Extended Data Fig. 1b) with hHER2 CAR-expressing mouse CD8<sup>+</sup> T cells induced dramatic cytotoxicity but not in the control CD8<sup>+</sup> T cells (Extended Data Fig. 1c and Supplementary Video 1), confirming that hHER2 is immunogenic in the B16 cell line. For in vivo assays, we used C57BL/6 hHER2 transgenic mice that overexpress the human *ERBB2* gene under the mouse mammary tumor virus promoter (obtained from Genentech<sup>10</sup>).

The current therapeutic T cell manufacturing process includes the selection and activation of T cells from human apheresis products using CD3/CD28 antibody beads and large clinical-scale T cell expansion with high concentrations of interleukin-2 (IL-2)<sup>11</sup>. Similarly,  $1 \times 10^7$  CD8<sup>+</sup> T cells from hHER2 transgenic mice were expanded in vitro, transfected

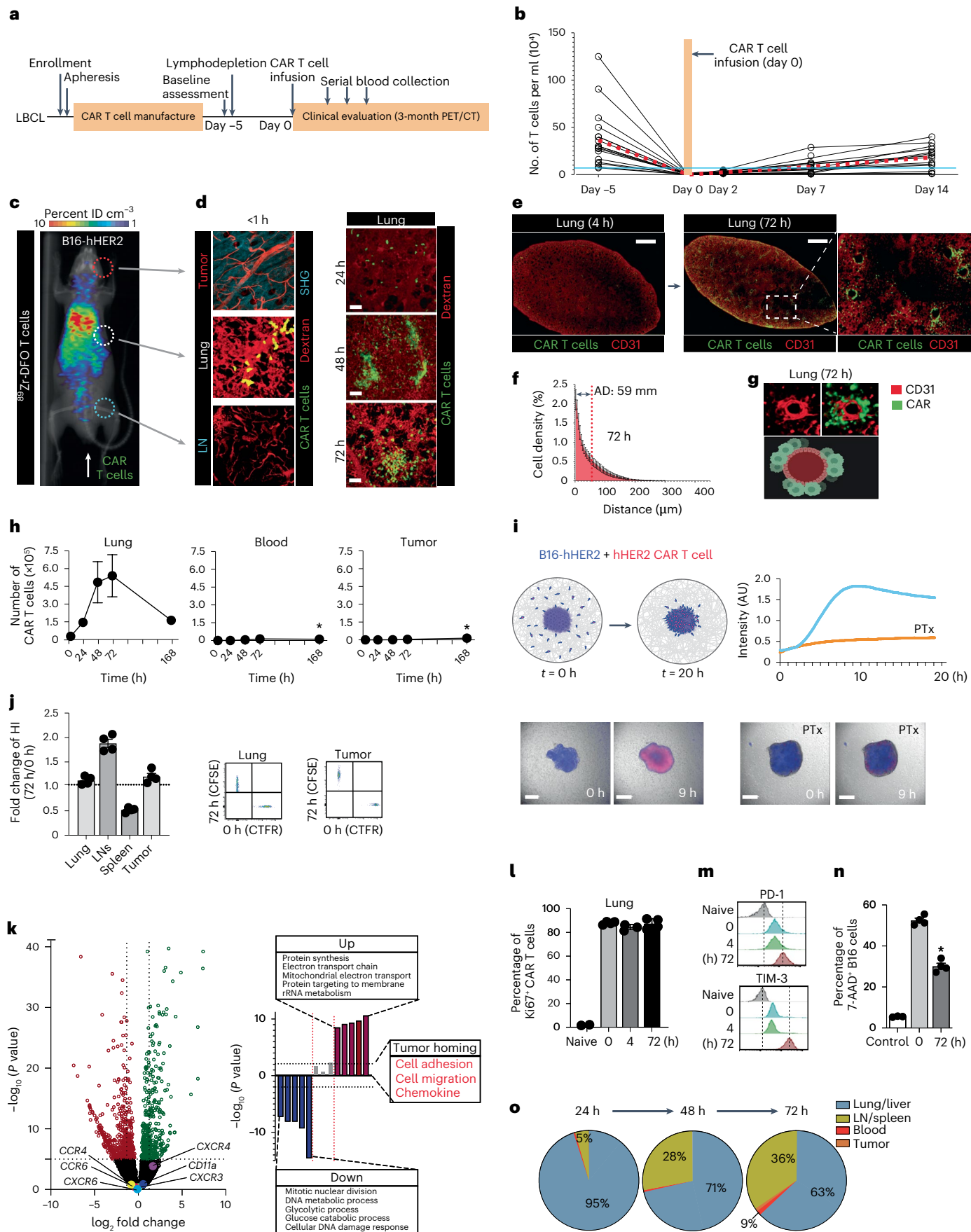
with the hHER2 CAR and transferred to hHER2 transgenic mice bearing B16-hHER2 tumors in the ear (Fig. 1c). The migration and distribution of intravenously infused CAR T cells were visualized by micropositron emission tomography/computed tomography (micro-PET/CT) imaging (Fig. 1c) and intravital multiphoton microscopy (IV-MPM) in different organs, such as the lung, lymph nodes (LNs) and tumors, of live recipient mice concurrent with the cell injection and for 72 h after injection (Fig. 1d). Initially (<1 h to 24 h after injection), very few cells appeared in tumors or LNs, with most CAR T cells instantly migrating to the lung (Fig. 1c,d and Supplementary Video 2). On days 2 and 3, we found that an increasing number of CAR T cells accumulated and formed clusters within the lung (Fig. 1d and Supplementary Video 3). Three-dimensional (3D) imaging of an optically cleared lung (Extended Data Fig. 1d) further confirmed that CART T cells actively accumulated in the lung 72 h after adoptive transfer (Fig. 1e), mainly along the perivascular space (Fig. 1f,g and Supplementary Video 4).

Flow cytometric quantifications also revealed similar results, demonstrating the maximal accumulation of CART T cells peaking on day 3, followed by a steady decrease over time to day 7 (Fig. 1h). In contrast to those in the lung (but consistent with clinical data<sup>1</sup>), nearly all CART T cells were undetectable in the peripheral blood after intravenous infusion. Seven days later, a small (but significant) number of CART T cells was observed in the blood and at the tumor site (Fig. 1h). Importantly, in vitro generated CART T cells preserved their directional migration patterns toward the target tumors (B16-hHER2 spheroids), which was completely abolished by pretreatment of the cells with pertussis toxin (PTx), an inhibitor of Gα<sub>i</sub> heteromeric G proteins that blocks chemotactic T cell migration (Fig. 1i and Supplementary Video 5). In addition, very few CART T cells were found to be localized within the vicinity of CD11c<sup>+</sup>MHC class II<sup>+</sup>tissue-resident antigen-presenting cells (Extended Data Fig. 2a), and there was no sign of B16 micrometastases in the lung during this period. Therefore, our data suggest that despite their tumor-specific trafficking ability following chemokine signals, the majority of intravenously transferred CART T cells quickly disappeared from the blood and homed to nonspecific peripheral tissues. Adoptive transfer of OT-I T cells into B16-ovalbumin (B16-OVA)-bearing mice showed similar T cell accumulation in the lung (Extended Data Fig. 2b), suggesting that in vitro stimulated T cells migrate into the non-inflamed lung after adoptive transfer even in the absence of CAR expression.

Next, we investigated whether CART T cells gradually lose the non-specific migration pattern and gain tumor-specific homing capability during retention in the lung. To test this, we first performed a competitive homing assay. hHER2 transgenic mice bearing B16-hHER2 tumors received equal numbers (1:1) of freshly prepared hHER2 CAR T cells (CART<sub>0</sub>) and CART T cells isolated from the lung 72 h after adoptive transfer (CART<sub>72</sub>). The ratio of CART<sub>72</sub> to CART<sub>0</sub> cells from various organs assessed 1 d after transfer revealed that CART<sub>72</sub> cells still readily reentered non-tumor-bearing lung tissue similar to CART<sub>0</sub> cells,

**Fig. 1 | CAR T cells accumulate in the lungs immediately after adoptive transfer.** **a**, Clinical protocol for CART T cell infusion (CTL019). LBCL, large B cell lymphoma. **b**, Blood T cell counts ( $N = 15$  participants). The red dashed line indicates the mean, and the blue line indicates the total blood lymphocyte counts (no linearity limit<sup>4</sup>). **c,d**, Visualization of early sequestration (0–1 h) of hHER2 CAR T cells after adoptive transfer with micro-PET/CT (<sup>89</sup>Zr-DFO-labeled T cells; **c**) or IV-MPM (red, dextran-labeled vessels; green, GFP-expressing CAR T cells; blue, second-harmonic generation (SHG); **d**). IV-MPM images on the right in **d** are from the lung at the indicated times after injection; scale bars, 50  $\mu$ m. **e**, Representative 3D imaging of CAR T cell accumulation in cleared lung 4 and 72 h after intravenous injection (red, blood vessels; green, CAR T cells); scale bars, 1 mm. **f**, Cell density curve and histogram of the distribution of T cells extravasated from the nearest blood vessel; AD, attraction distance. **g**, Three-dimensional image of GFP-expressing CAR T cells and CD31-labeled vessels. **h**, The number of injected CAR T cells in the lung, blood and tumor at the indicated times. \* $P < 0.0001$ . **i**, In vitro migration of hHER2 CAR T cells (red) to a

hHER2-B16-BFP tumor spheroid (blue); scale bars, 100  $\mu$ m; AU, arbitrary units. **j**, CAR T cells from the lung 72 h after intravenous injection ( $t_{72}$ ; CFSE) and newly in vitro activated CAR T cells ( $t_0$ ; CTFR) were cotransferred (1:1 mix), and the fold change in the homing index (HI) was analyzed 24 h after injection ( $n = 4$ ; 13 mice per experiment). **k**, Volcano plot and signaling pathway from RNA-sequencing analysis in CAR T cells ( $t_{72}$  versus  $t_0$ ). **l**, Percentage of Ki67<sup>+</sup> cells in in vitro activated CAR T cells (0 h) or CAR T cells isolated from the lung after intravenous injection (4 and 72 h). **m**, Flow cytometry results of PD-1 and TIM-3 expression levels on naive and CAR T cells isolated from the lung at the indicated times after injection. **n**, The cytotoxicity of CAR T cells (PBS,  $t_{72}$  and  $t_0$ ) against B16-hHER2. **o**, The proportion of CAR T cells distributed across different organs after injection. The images in **d** and **e** are representative of five mice. The data in **l** and **n** are representative of three experiments with  $n = 3$  per group, and the data in **f** and **o** are from  $n = 3$  mice per group. Results in **h,j,l** and **n** are shown mean  $\pm$  s.e.m. Data were analyzed by ordinary one-way analysis of variance (ANOVA) with Tukey's multiple-comparison post hoc test (**h**) or two-tailed Student's *t*-test (**n**).



suggesting that lung retention for 72 h did not diminish the nonspecific migration pattern (Fig. 1j). More importantly, CART<sub>72</sub> cells did not show a greater ability to enter tumors than CART<sub>0</sub> cells (Fig. 1j). Although the transcriptional profiles across the genome showed substantial differences between CART<sub>0</sub> and CART<sub>72</sub> cells (Extended Data Fig. 2c), the data demonstrated that the expression of genes controlling T cell adhesion, motility and tumor-specific homing was not significantly changed during lung retention (Fig. 1k).

In addition, the majority of CAR T cells in the lung exhibited a higher frequency of Ki67 (Fig. 1l) and Extended Data Fig. 2d,e) with diminished expression of inflammatory cytokines (Extended Data Fig. 2h). Although Ki67 is often used as an indicator of the proliferative capability of T cells, it is also expressed on recently divided and terminally exhausted T cell populations with decreased effector functions<sup>12,13</sup>. Indeed, both CART cells (CART<sub>72</sub>) and OT-IT cells drastically upregulated PD-1 and TIM-3 expression after 72 h of lung retention, suggesting that these cells may have been functionally exhausted (Fig. 1m and Extended Data Fig. 2g). Furthermore, CART<sub>72</sub> cells exhibited decreased cytotoxicity against B16-hHER2 cells (Fig. 1n). Therefore, during nonspecific retention in the lung, these CAR T cells fail to functionally reprogram to raise their capacity to migrate toward target tumor sites but upregulate exhaustion markers and decrease cytotoxic effector function. Notably, the number of CAR T cells gradually increased in the LNs and spleen after 72 h (Fig. 1o). CAR T cells that arose in the LNs after 72 h showed improved cytotoxicity against B16-hHER2 cells compared to CAR T cells sequestered in the lung (Extended Data Fig. 2h). Furthermore, the enhanced effector functions of CAR T cells in the LNs after 72 h coincided with the downregulation of PD-1 and TIM-3 expression (Extended Data Fig. 2i). These results indicate a limited role of lung retention in CAR T cell activation and suggest that a shift in the dynamic equilibrium of CAR T cell positions between non-tumor-bearing tissues (such as the lung and liver) and the circulation (the blood/spleen and LNs) after intravenous transfer may have important impacts on anticancer effector functions of CAR T cells<sup>3,14</sup>.

### In vivo CRISPR screen identifies a regulator of CAR T cell migration

To identify genes that cause CAR T cell migration to nonspecific sites in vivo, we used libraries of single guide RNAs (sgRNAs) targeting 1,316 genes that are differentially expressed between in vitro activated and naïve CD8<sup>+</sup> T cells (Fig. 2a and Extended Data Fig. 3a,b). The sgRNA plasmid library prepared with 5 sgRNAs per gene and approximately 300 negative-control sgRNAs was verified for successful clones and a log-normal distribution (Extended Data Fig. 3c). The plasmid library was then packaged into retrovirus, and expression of red fluorescent protein-positive (RFP<sup>+</sup>) signals was confirmed by flow cytometry to ensure adequate viral transfection in CD8<sup>+</sup> T cells isolated from OT-I/Rosa26<sup>LSL-GFP</sup>Cas9 mice<sup>15</sup> (Extended Data Fig. 3d). The double-positive populations of sgRNA (RFP<sup>+</sup>) and Cas9 (green fluorescent protein-positive (GFP<sup>+</sup>)) OT-I cells (Extended Data Fig. 3d) were adoptively

transferred into B16-OVA-bearing congenic recipient mice (Fig. 2a). At 24 h after infusion, sgRNA<sup>+</sup>Cas9<sup>+</sup> OT-I cells were isolated from different organs and evaluated. To ensure sufficient library coverage ( $>500\times$ ), we limited the number of adoptively transferred Cas9-OT-I cells to  $3.5 \times 10^6$  per mouse and  $0.35 \times 10^6$  after taking from each organ compartment (~50 cells per sgRNA). For our screens, we predicted that infused sgRNA<sup>+</sup>Cas9<sup>+</sup> OT-I cells were recruited into two different tissue compartments: T cells located in the non-tumor-bearing lung and liver (termed T<sub>sequestered</sub> cells) and T cells reemerged in the circulation before their recruitment to the tumor site (termed T<sub>migratory</sub> cells). To interrogate the genetic landscape of CAR T cell migration, we explored our dataset to identify genes with differential fitness effects in T<sub>sequestered</sub> versus T<sub>migratory</sub> cell populations relative to control cells using the drugZ algorithm<sup>16</sup> (Fig. 2b and Extended Data Fig. 3e,f). This analysis revealed that 124 genes in the T<sub>sequestered</sub> cell population and 207 genes in the T<sub>migratory</sub> cell population affect T cell migration in vivo (false discovery rate (FDR) < 5%) and identified key genes that may drive CAR T cells to the non-tumor-bearing tissues (Fig. 2b). Among these, St3gal1 and Spc24 were the strongest hits in repressing the T<sub>sequestered</sub> cell population (Fig. 2c,d).

ST3GAL1 is a Golgi membrane-bound sialyltransferase that adds sialic acid residues in an  $\alpha$ 2,3-linkage to galactose-containing substrates (Gal- $\beta$ 1,3-GalNAc)<sup>17</sup>. Importantly, ST3GAL1 regulates cell migration and lymphocyte differentiation<sup>18–20</sup>. SPC24 is a nuclear protein involved in the formation of the kinetochore complex, which mediates chromosome segregation during mitosis and cell cycle progression<sup>21</sup>. In in vitro activated CD8<sup>+</sup> T cells, quantitative PCR with reverse transcription (RT-qPCR) analyses revealed that the genes associated with the expression of ST3GAL1 and SPC24 were significantly increased in both human and mouse activated CD8<sup>+</sup> T cells (Fig. 2e,g). Consistently, the protein expression levels of both ST3GAL1 and SPC24 were also elevated during the activation of human and mouse CD8<sup>+</sup> T cells (Fig. 2f,h). To examine whether these proteins are directly involved in CAR T cell migration, we cloned sgRNAs targeting St3gal1 and Spc24 into the retroviral CRISPR vector (sgSt3gal1 and sgSpc24). We then transduced Cas9 hHER2 CAR T cells and confirmed successful knock-out (KO) of the target proteins (Fig. 2i). Deletion of St3gal1 or Spc24 in CAR T cells did not change CAR-mediated cytotoxicity (Fig. 2j), but it significantly reduced nonspecific migration patterns into the lung and liver (Fig. 2k). Notably, sgSt3gal1-infected Cas9 CAR T cells, but not sgSpc24-infected CAR T cells, dramatically improved their retention in the circulation (the spleen and LNs) after intravenous transfer (Fig. 2k). These data suggest that ST3GAL1 may play an important role in the regulation of both nonspecific sequestration and tumor-specific migration patterns of CAR T cells.

### ST3GAL1 regulates LFA-1-mediated CAR T cell migration

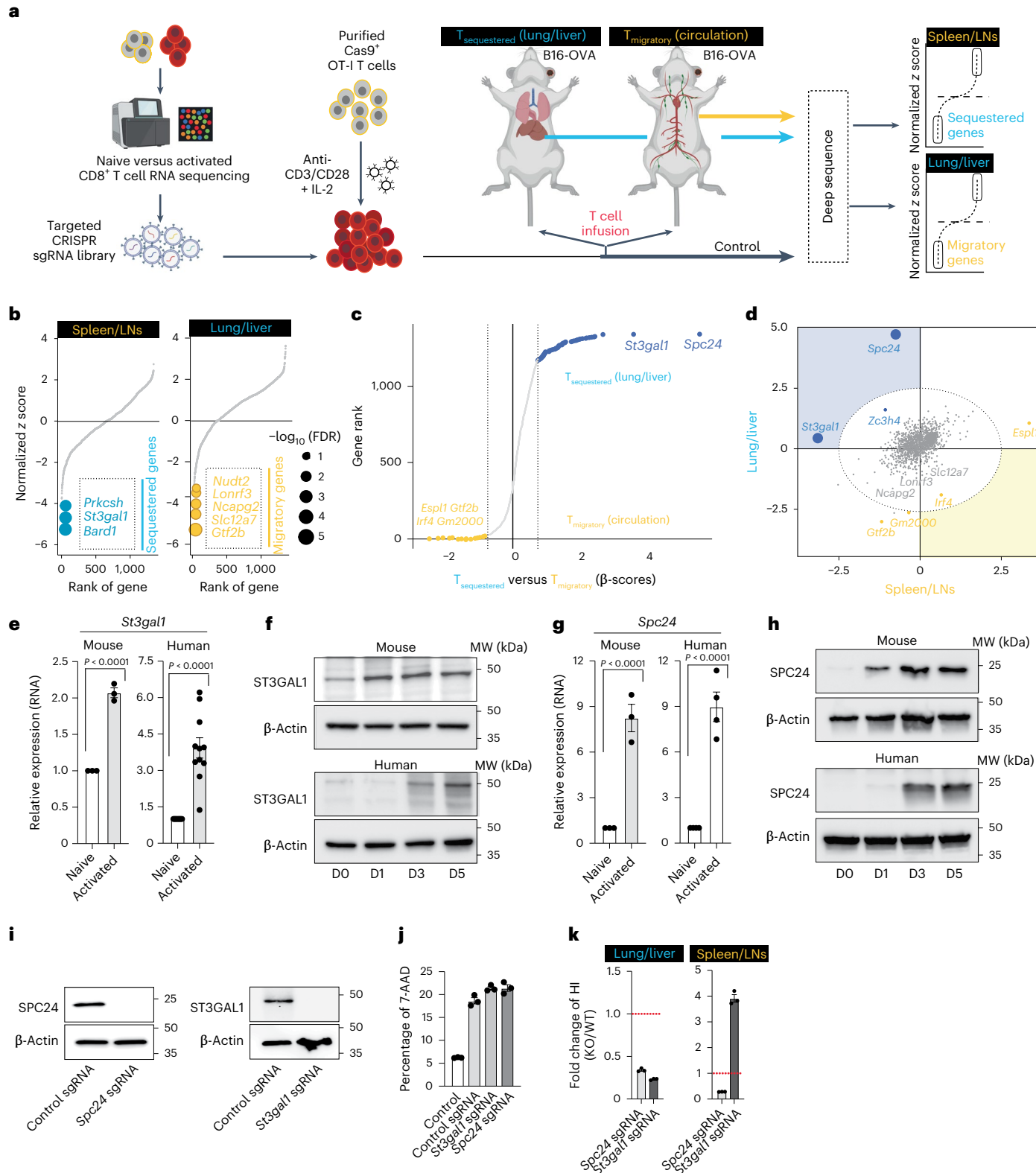
To further dissect the molecular mechanism by which ST3GAL1 regulates CAR T cell migration, we first performed flow cytometry analyses. In vitro activated mouse and human CD8<sup>+</sup> T cells showed augmented cell

**Fig. 2 | A regulator of CAR T cell migration identified using a CRISPR screen.** **a**, Schematic for the development of a pooled in vivo CRISPR screening platform in mouse CD8<sup>+</sup> T cells (created with BioRender.com). **b**, Rank-ordered normalized z score of the  $\beta$ -values for all three OT-IT cell distribution screens in B16-OVA-bearing mice; yellow, migratory genes; blue, sequestered genes. The top three sequestered and the top five migratory genes are indicated. **c**, Gene rank based on the difference in  $\beta$ -scores across sequestered and migratory conditions. **d**, Sectorized scatter plot of gene-level  $\beta$ -values from T<sub>sequestered</sub> versus T<sub>migratory</sub> cell populations isolated from B16-OVA-bearing mice. Significant migratory genes and sequestered gene signatures (FDR < 5%) are colored yellow and blue, respectively; ellipse (gray dashed lines), 5% FDR threshold delineated by normal ellipse fit to differential scores. **e**, RT-qPCR of St3gal1 in mouse and human CD8<sup>+</sup> T cells (naive versus activated) compared to three averaged housekeeping genes

( $n = 3–11$ ). **f**, Expression levels of ST3GAL1 in activated CD8<sup>+</sup> T cells (from days 0 to 5 (D0 to D5)).  $\beta$ -Actin served as the loading control; MW, molecular weight. **g**, RT-qPCR of Spc24 in mouse and human CD8<sup>+</sup> T cells (naive versus activated) compared to three averaged housekeeping genes ( $n = 3–4$ ). **h**, Expression levels of SPC24 in activated CD8<sup>+</sup> T cells (from days 0 to 5).  $\beta$ -Actin served as the loading control. **i**, Expression levels of SPC24 and ST3GAL1 in Cas9 hHER2 CAR T cells with sgSpc24 and sgSt3gal1, respectively.  $\beta$ -Actin served as the loading control. **j**, Cytotoxicity of CAR T cells (PBS, sgSpc24 cells and sgSt3gal1 cells) against B16-hHER2 ( $n = 3$ ). **k**, The distribution of CAR T cells with (WT; CTFR) and without (KO; CFSE) Spc24 or St3gal1 24 h after injection ( $n = 3$ ). The fold change in the homing index, as determined by  $(KO_{\text{sample}}/WT_{\text{sample}})/(KO_{\text{input}}/WT_{\text{input}})$ , is shown. Results in **e**, **g**, **j** and **k** are shown as mean  $\pm$  s.e.m. The data in **j** and **k** reflect three independent experiments. Data in **e** and **g** were analyzed by two-tailed Student's t-test.

surface binding of *Maackia amurensis* lectin-II (MAL-II), a plant lectin that preferentially binds  $\alpha$ 2,3-linked sialic acid<sup>22</sup> (Fig. 3a). In addition, deletion of *St3gal1* in activated CD8<sup>+</sup> T cells significantly reduced the cell surface binding of MAL-II, further confirming that the increased sialylated glycan activity is associated with ST3GAL1 overexpression (Fig. 3b). To identify the T cell glycoproteins bearing ST3GAL1-specific  $\alpha$ 2,3-sialylated glycans, we immunoprecipitated MAL-II-binding

glycoproteins from CD8<sup>+</sup> T cells. Analysis of MAL-II immunoprecipitates revealed that a prominent protein of ~90 kDa was associated with MAL-II, and the protein signal was preferentially enriched in immunoprecipitates obtained from activated T cells compared to naive T cells (Fig. 3c). The 90-kDa species was identified as CD18, as determined by mass spectrometry (MS; Fig. 3c, Extended Data Fig. 4a and Supplementary Table 1). To further validate whether the interaction was specific to



sialic acid, we treated the CD8<sup>+</sup> T cell lysates with neuraminidase to remove sialic acids. Neuraminidase treatment caused a detectable change in the electrophoretic mobility of CD18 in SDS-PAGE (Fig. 3d). The removal of N-glycans by PNGase F treatment further shifted CD18 to a lower molecular weight (Fig. 3d). These findings suggested that sialylation of CD18 is likely an O-linked sialylated glycoprotein catalyzed by ST3GAL1. Consistent with this prediction, MAL-II pulldown showed that binding of MAL-II to CD18 was decreased after *St3gal1* silencing, while total CD18 protein expression remained the same (Fig. 3e). To identify potential O-glycosylation sites, CD18 immunoprecipitates were treated with PNGase F (to remove N-glycans) and digested using trypsin, followed by liquid chromatography–tandem MS (LC–MS/MS) analysis. The results of peptide mass spectra from CD18 revealed O-glycosylation on T256 (Extended Data Fig. 4b and Supplementary Table 2). In the crystal structure of the LFA-1 headpiece<sup>23</sup>, the O-glycan site locates within the βI domain, which plays a key role in determining ligand binding specificity and affinity of LFA-1 (Extended Data Fig. 4c)<sup>24</sup>. Therefore, our data suggest that overexpression of ST3GAL1 in activated T cells causes the early accumulation of in vitro activated T cells within the pulmonary circulation via glycosylation of LFA-1, the dominant CD18 integrin expressed on CD8<sup>+</sup> T cells.

Indeed, the nonspecific accumulation of CAR T cells in the lung was significantly reduced by treatment with anti-LFA-1 (Fig. 3f). Compared to wild-type (WT) CAR T cells, *Lfa-1*-KO CAR T cells also showed a marked decrease in lung accumulation, with the majority of CAR T cells remaining in the spleen (Fig. 3g). Consistent with previous findings with T cell blasts<sup>25,26</sup>, the accumulation of CAR T cells in the non-inflamed lung was not sensitive to PTx (Fig. 3f), suggesting ‘PTx-insensitive’ and ‘LFA-1-dependent’ accumulation of in vitro activated CAR T cells in non-inflamed tissues. Note that the concentrations of antibody to LFA-1 and PTx used were determined based on previous publications<sup>27,28</sup> and from our studies in which they significantly blocked T cell entry into draining LNs (dLN; Extended Data Fig. 5a).

In in vitro assays, the migration of naive T cells was strictly dependent on chemokine stimulation (Fig. 3h). However, similar to the migration pattern observed in vivo, activated CD8<sup>+</sup> T cells migrated on ICAM-1 spontaneously in the absence of chemokines (Fig. 3h and Supplementary Video 6). Key effector T cell chemokines, including CXCL12 and CXCL10, did not further enhance the migration of activated T cells (Extended Data Fig. 5b–d). Furthermore, neither PTx nor another pan-GPCR inhibitor gallein (Gβγ subunit inhibitor)<sup>29</sup> blocked spontaneous T cell migration on ICAM-1 (Fig. 3h). Consistent with cell migration under static conditions, activated CD8<sup>+</sup> T cells adhered and migrated on ICAM-1-coated surfaces (Extended Data Fig. 5e–g and Supplementary Video 7) or on a monolayer of primary mouse endothelial cells (Extended Data Fig. 5h) in a flow chamber under high shear conditions (1 dyn cm<sup>-2</sup>) that can remove any autocrine and/or paracrine chemotactic molecules released by migrating T cells. Therefore, our data further confirm that in vitro activated CD8<sup>+</sup> T cells can migrate on ICAM-1 using LFA-1 in the absence of chemokine stimulation. Selective depletion of

ST3GAL1 in CD8<sup>+</sup> T cells resulted in a significant decrease in spontaneous and chemokine-independent T cell migration on ICAM-1, but, more importantly, it allowed chemokine-dependent T cell migration on ICAM-1 (Fig. 3i), suggesting that there is a direct relationship between ST3GAL1 functions and ‘chemokine-independent/LFA-1-mediated’ accumulation of CAR T cells in nonspecific tissue sites.

### ST3GAL1 does not directly activate T cell surface LFA-1

We first addressed whether ST3GAL1 overexpression in activated CD8<sup>+</sup> T cells in vitro was associated with changes in LFA-1 affinity (conformation change). To determine whether in vitro T cell activation induces the constitutive activation of LFA-1 affinity, we performed LFA-1 fluorescence resonance energy transfer (FRET) assays with T cells isolated from LFA-1 FRET mice that express monomeric yellow fluorescent protein (mYFP) and monomeric cyan fluorescent protein (mCFP) tagged to the cytosolic tails of CD11a and CD18, respectively<sup>30</sup> (Fig. 3j). When LFA-1 is in the high-affinity state, the cytosolic tails are separated, leading to low-efficiency FRET. In this way, FRET efficiency is correlated with integrin affinity<sup>30,31</sup>. The results suggest that LFA-1 conformation remains in the low-affinity state under basal conditions in activated CD8<sup>+</sup> T cells (Fig. 3j).

Next, scanning electron microscopy (SEM) of in vitro activated CD8<sup>+</sup> T cells confirmed a dramatic increase in cell size with a significant increase in microvilli density (Fig. 3k). Thus, we speculated that adhesion and migration of activated CD8<sup>+</sup> T cells on ICAM-1 in the absence of chemokines may simply be induced by ST3GAL1-mediated modification of LFA-1 topography and clustering (avidity) on the increased cell membrane surface<sup>31</sup>. Indeed, the total internal reflectance (TIRF) microscopy:epifluorescence (epi) ratio for LFA-1 (Extended Data Fig. 6a) was lower in activated cells before spreading, indicating the distal location of LFA-1 relative to the surface topography (Fig. 3l). As cells spread on ICAM-1, the membrane flattened, leading to high concentrations of LFA-1 being redistributed into the contact site with ICAM-1 substrate (a higher TIRF:epi ratio). Under this condition, however, we detected the same ratio of LFA-1 accumulation at the cell–ICAM-1 interface in both activated and naive T cells (Fig. 3l and Extended Data Fig. 6b). These observations imply that topographical remodeling and clustering (avidity) of LFA-1 that occurs with T cell activation is unlikely to affect the spontaneous adhesion and migration of activated T cells on ICAM-1.

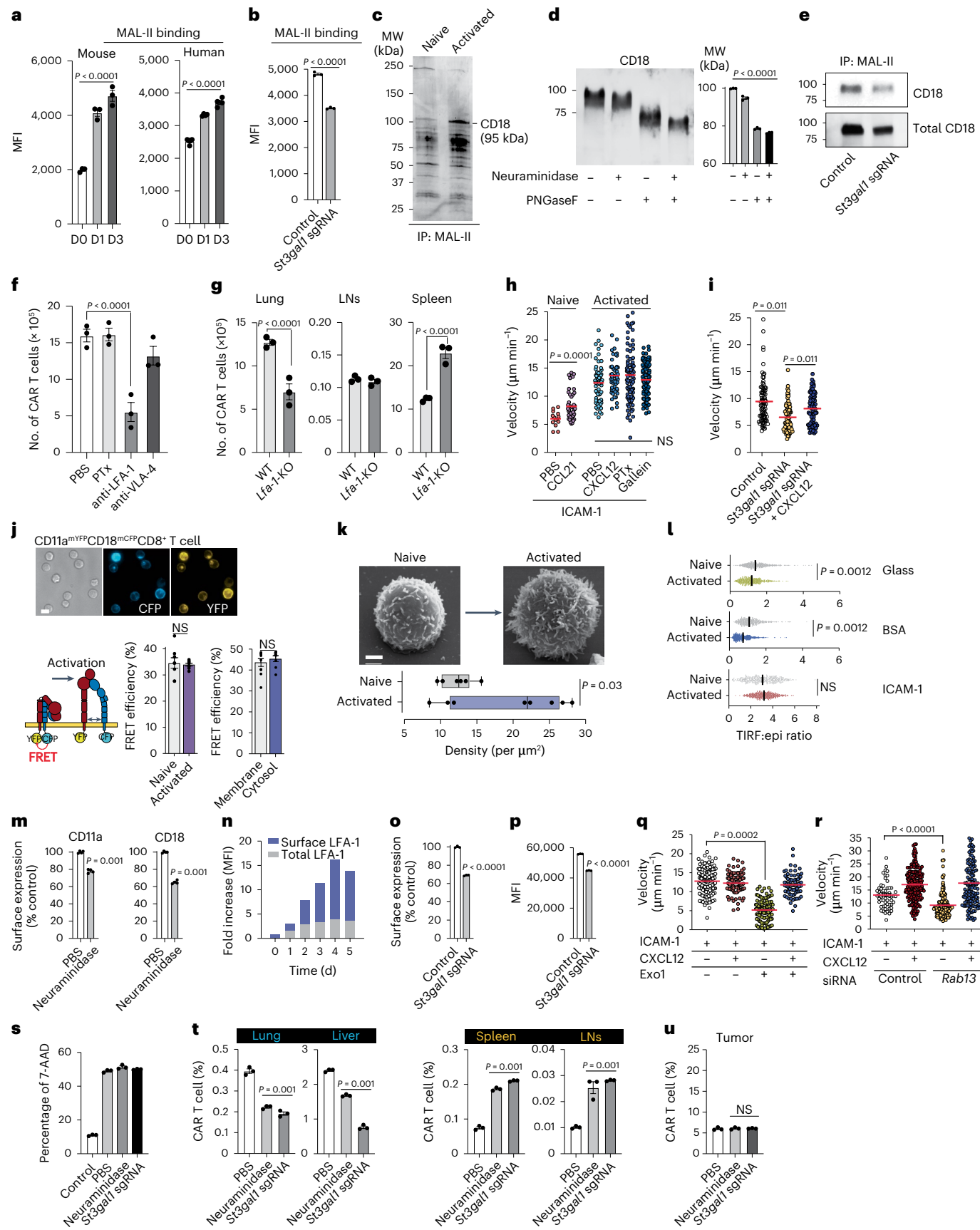
To screen potential mechanisms for the LFA-1-mediated spontaneous T cell migration on ICAM-1, we next turned our attention to integrin recycling. Importantly, desialylation of in vitro activated CD8<sup>+</sup> T cells by neuraminidase caused a significant increase in endocytosis of cell surface LFA-1 (Fig. 3m), suggesting that glycosylation of cell surface LFA-1 by ST3GAL1 may inhibit endocytic recycling of LFA-1, causing a sustained increase in cell surface expression of LFA-1. Indeed, we observed that the surface level of LFA-1 increased 2.5-fold 48 h after T cell activation and that total LFA-1 expression remained stable in the following days (Fig. 3n). In addition, the endocytosis of LFA-1 was

**Fig. 3 | ST3GAL1 regulates LFA-1-mediated CAR T cell migration.** **a, b**, MAL-II binding to CD8<sup>+</sup> T cells (**a**) and *St3gal1*-KO CAR T cells (**b**). **c**, Immunoprecipitation of MAL-II-binding proteins in CD8<sup>+</sup> T cells; IP, immunoprecipitation. **d**, Western blot of the activated CD8<sup>+</sup> T cell lysates after enzyme treatments. In the graph, each bar represents the calculated molecular weight of protein bands. **e**, Immunoprecipitation of MAL-II binding CD18 in activated CD8<sup>+</sup> T cells. **f**, Recruitment of CAR T cells into lung tissue ( $n = 3$  mice per group). **g, h**, The numbers of WT or *Lfa-1*(CD11a)-KO CAR T cells 24 h after CAR T cell injection ( $n = 3$ ). **i**, In vitro CD8<sup>+</sup> T cell migration on ICAM-1-coated plates ( $n = 3$  mice;  $n = 13\text{--}38$  individual cells per mouse). **j**, In vitro activated CD8<sup>+</sup> T cell migration on ICAM-1-coated plates ± CXCL12 ( $n = 3$  mice;  $n = 10\text{--}57$  individual cells per mouse). **k**, LFA-1 FRET assay with CD11a–mYFP and CD18–mCFP; scale bars, 5  $\mu\text{m}$  ( $n = 3$  mice;  $n = 20\text{--}40$  individual cells per condition). **l**, Density of microvilli of CD8<sup>+</sup> T cells by SEM ( $n = 6\text{--}8$ ); scale bars, 1  $\mu\text{m}$ . **m**, Ratio of the TIRF microscopy signal from LFA-1 accumulation of CD8<sup>+</sup> T cells at sites of contact with the surface

( $n = 3$ ). **m**, Changes in the endocytosis of LFA-1 in CD8<sup>+</sup> T cells after treatment with α2,3-neuraminidase ( $n = 3\text{--}4$ ). **n**, Time course of surface and intracellular LFA-1 expression. **o, p**, Changes in the endocytosis (**o**) and cell surface expression (**p**) of LFA-1 in CAR T cells ( $n = 3$ ). **q, r**, Migration of activated CD8<sup>+</sup> T cells pretreated with Exo1 (**q**) or transfected with *Rab13* siRNA (**r**;  $n = 3$  mice;  $n = 20\text{--}68$  individual cells per mouse). **s**, The cytotoxicity of CAR T cells against B16-hHER2 ( $n = 3$ ). **t, u**, The percentage of hHER2 CAR T cells in peripheral tissue sites (**t**) and tumors (**u**) 24 h after adoptive transfer ( $n = 3$  mice per group). Results are shown as mean fluorescence intensity (MFI)  $\pm$  s.e.m. (**a** and **b**) and as mean  $\pm$  s.e.m. (**c, f–m, o** and **p**). All data and representative images reflect three independent experiments. Statistical analyses were performed using a one-way ANOVA with a Bonferroni post hoc test (**a–c, h, i, q** and **r**), two-sided Mann–Whitney test (**f, t** and **u**), two-sided, unpaired Student’s *t*-test (**g** and **j**) or two-tailed Student’s *t*-test (**k–m, o** and **p**); NS, not significant.

significantly increased by genetically deleting *St3gal1* (Fig. 3o), leading to a downregulation in cell surface LFA-1 expression on activated CD8<sup>+</sup> T cells (Fig. 3p). Note that the enhanced endocytic recycling of

LFA-1 in *St3gal1*-KO CD8<sup>+</sup> T cells is closely associated with a decrease in spontaneous and chemokine-independent T cell migration but allows chemokine-dependent T cell migration on ICAM-1 (Fig. 3i). Consistent



with these results, promoted endocytic trafficking of membrane LFA-1 by cell treatment with Exo1 (ref. 32; an inhibitor of exocytic vesicular transport) or short interfering RNA (siRNA)-mediated downregulation of *Rab13* expression<sup>33</sup> (which can inhibit exocytic transport of LFA-1) resulted in a significant decrease in spontaneous and chemokine-independent T cell migration on ICAM-1, but, more importantly, it enhanced chemokine-dependent T cell migration on ICAM-1 (Fig. 3q,r). Therefore, our data suggest that the inhibition of ST3GAL1-mediated protein glycosylation can normalize the LFA-1 endocytic recycling process and prevent nonspecific T cell migration *in vivo*, thus holding significant therapeutic potential to potentiate the tumor-specific migration and antitumor function of CAR T cells.

To test whether reducing ST3GAL1 expression and/or inhibition of its functions can drive CAR T cells to their desired tissue locations and improve therapeutic efficacy, we first confirmed that treatment of hHER2 CAR T cells with neuraminidase and sgSt3gall1 infection of Cas9 hHER2 CAR T cells (*St3gall1* KO) do not alter CAR-mediated cytotoxicity (Fig. 3s). As we expected, both deletion of *St3gall1* in CAR T cells and neuraminidase treatment suppressed nonspecific T cell retention in the lung and liver and significantly improved CAR T cell retention in the circulation (the spleen and LNs) after intravenous transfer (Fig. 3t). However, unlike our prediction, *St3gall1* KO and pretreatment of CAR T cells with neuraminidase before intravenous transfer did not promote more robust tumor-specific migration (Fig. 3u). This result suggests that the general inhibition of ST3GAL1-mediated cell surface sialylation may be a blunt tool, which not only reduces nonspecific tissue sequestration but also negatively impacts the tissue-specific homing of effector T cells<sup>17</sup>.

#### Spontaneous migration of T cells is associated with βII-spectrin

LFA-1 binding to ICAM-1 initiates outside-in signals that reorganize the cell cytoskeleton to regulate adhesion turnover via integrin endocytosis and/or recycling<sup>34</sup>. Therefore, we hypothesize that the reduced LFA-1 endocytic process by ST3GAL1-mediated glycosylation can be counterbalanced by promoting cytoskeletal force that can drive greater LFA-1 endocytosis in *in vitro* activated T cells. To screen for potential cytoskeletal molecules mediating LFA-1 endocytosis and surface distribution after ligand binding, LFA-1 immunoprecipitates obtained from ICAM-1-bound T cells (in the absence of chemokine stimulation) were analyzed by MS. We discovered that three cytoskeletal molecules, αII- and βII-spectrin and non-muscle myosin heavy chain IIA (MyH9), were associated with LFA-1 in T cells (Fig. 4a). Western blotting revealed that these three LFA-1-associated molecules were highly expressed in naive T cells (Fig. 4b). The expression levels of αII-spectrin and MyH9 remained constant after T cell activation; however, βII-spectrin expression was dramatically downregulated during *in vitro* activation of CD8<sup>+</sup> T cells (Fig. 4b).

Spectrin regulates LFA-1 clustering in T cells during the formation of immunological synapses<sup>35</sup>. Although the dramatic downregulation of βII-spectrin during T cell activation hinted at a possible role for

βII-spectrin in the functions of LFA-1 in activated T cells, it was unclear whether there was a direct relationship between βII-spectrin and LFA-1 redistribution in T cells. To investigate this relationship, we transiently transfected activated CD8<sup>+</sup> T cells prepared from CD11a-mYFP knock-in mice<sup>36</sup> with βII-spectrin. Fluorescence recovery after photobleaching (FRAP) assays revealed that restoration of βII-spectrin expression in activated CD8<sup>+</sup> T cells did not alter LFA-1 lateral mobility in the cell membrane ( $t_{1/2} = 91.3 \pm 21.7$  versus  $t_{1/2} = 91.2 \pm 23.3$  with/without βII-spectrin expression; Fig. 4c). Instead, the cell membrane LFA-1 FRAP analysis showed a significant decrease in the immobile LFA-1 fraction with βII-spectrin expression ( $33 \pm 5\%$  versus  $9 \pm 9\%$ ). The fact that the membrane mobile fraction of LFA-1 increases without a change in the membrane lateral mobility suggests that forced βII-spectrin expression in *in vitro* activated CD8<sup>+</sup> T cells causes greater dynamic endocytic recycling of LFA-1 (refs. 37,38). Indeed, live video imaging and TIRF analysis of CD11a-mYFP-expressing naive and activated CD8<sup>+</sup> T cells binding to the ICAM-1-coated surface revealed that both LFA-1-mediated cell spreading rate ( $\mu\text{m}^2 \text{s}^{-1}$ ) and maximum contact area ( $\mu\text{m}^2$ ) on ICAM-1 were significantly increased after T cell activation (Fig. 4d,e and Supplementary Video 9), but when βII-spectrin expression was restored in activated CD8<sup>+</sup> T cells (by transfection), the spreading rate and total spreading area were significantly decreased on ICAM-1-coated dishes compared to WT activated CD8<sup>+</sup> T cells (Fig. 4d,e and Supplementary Video 9). Indeed, transient transfection of activated CD8<sup>+</sup> T cells with βII-spectrin reduced chemokine-independent migration on ICAM-1 (Fig. 4f and Supplementary Video 8), but, more importantly, it preserved the chemokine-dependent (and PTx-sensitive) pattern of T cell migration on ICAM-1, which was comparable to that of naive CD8<sup>+</sup> T cells (Fig. 4f).

In conclusion, our data suggest that the restoration of βII-spectrin expression in *in vitro* activated CD8<sup>+</sup> T cells normalizes overall cell adhesiveness to ICAM-1 and migration by reversing the ST3GAL1-induced downregulation of LFA-1 endocytic process (Fig. 4g). To further address the functions of βII-spectrin in LFA-1 regulation, we generated a conditional βII-spectrin transgenic mouse (*GFP-Rosa<sup>βII-spectrin</sup>* mouse) to restore βII-spectrin expression only in activated CD8<sup>+</sup> T cells under the control of the *Rosa26* locus in a Cre recombinase-dependent manner (Extended Data Fig. 7a). Treatment of these T cells with the membrane-permeable TAT-Cre fusion protein conjugated with a nuclear localization sequence<sup>39</sup> during *in vitro* activation led to significant expression of βII-spectrin in hHER2 CAR T cells (Fig. 4h). The forced expression of βII-spectrin in hHER2 CAR T cells did not alter their effector functions, including interferon-γ (IFNγ) and tumor necrosis factor (TNF) production or CAR-mediated cytotoxicity (Extended Data Fig. 7b-d). Consistent with our predicted model (Fig. 4g), transmission electron microscopy images of LFA-1 immunostaining at the contacts between hHER2 CAR T cells and endothelial cells revealed that the overexpression of βII-spectrin in T cells reduced LFA-1 accumulation at contact sites (Fig. 4i). The decreased LFA-1 distribution at the contact sites between the ICAM-1-coated surface

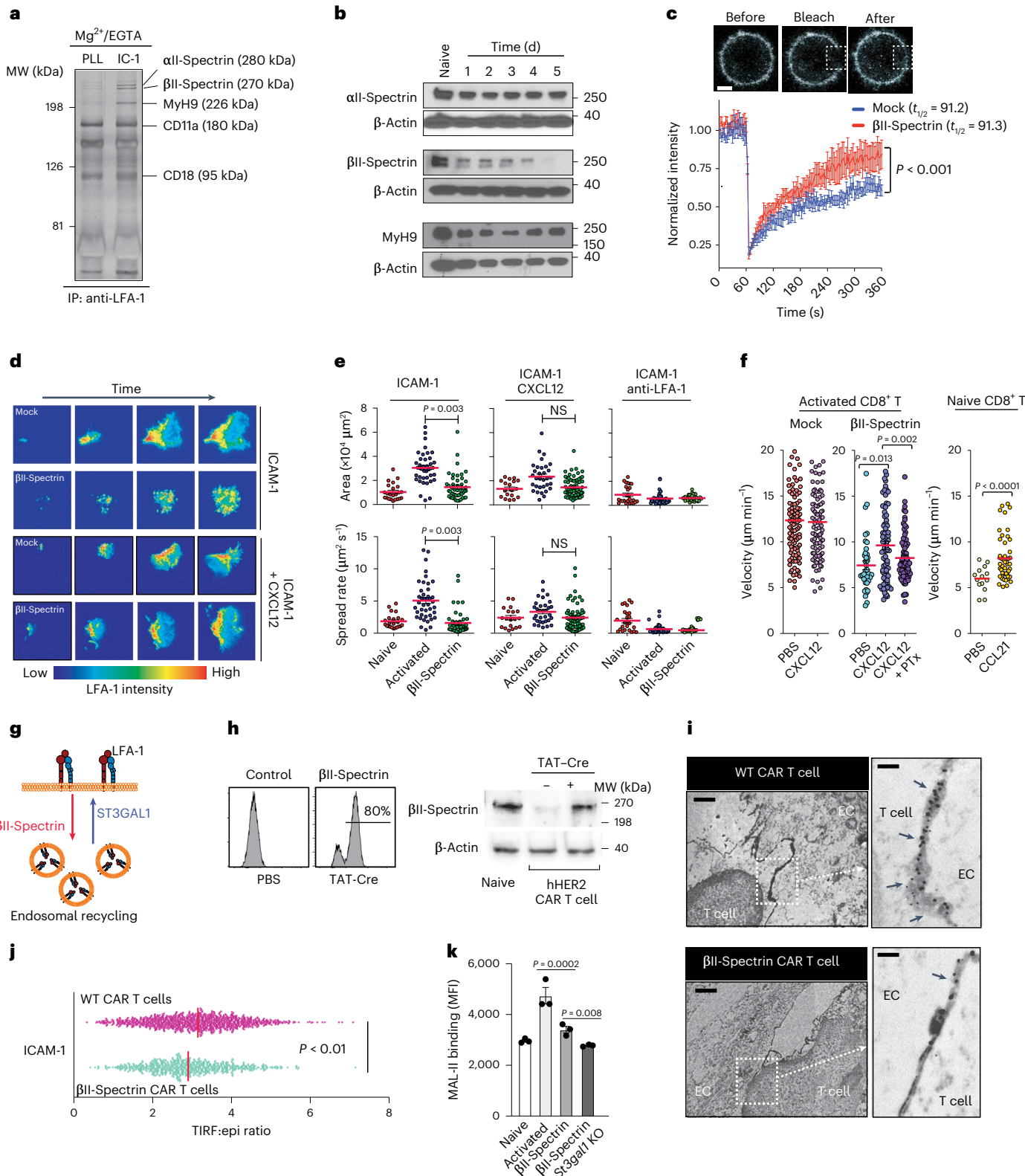
#### Fig. 4 | ST3GAL1–βII-spectrin axis controls LFA-1-mediated T cell migration.

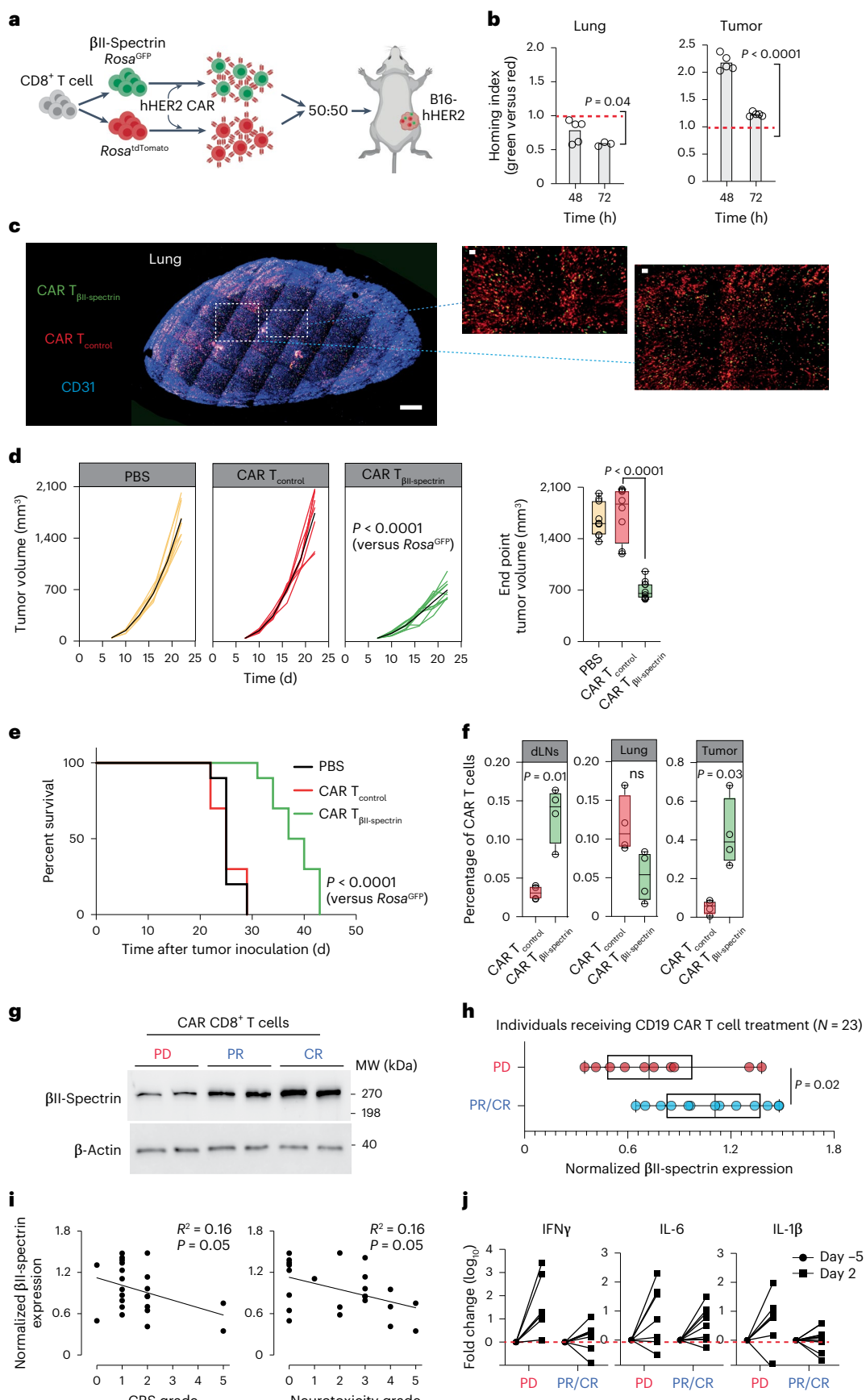
**a**, LFA-1 immunoprecipitates obtained from human T cells bound on ICAM-1 (IC-1)-coated or poly-L-lysine (PLL)-coated coverglass. LFA-1-associated proteins were identified by silver staining and MS. **b**, Expression levels of αII-spectrin, βII-spectrin and MyH9 in activated T cells (from days 0 to 5). β-Actin served as the loading control. **c**, A confocal FRAP experiment with activated CD11a-mYFP CD8<sup>+</sup> T cells ( $n = 3$ ); scale bars, 1 μm. **d,e**, Representative TIRF microscopy images of activated CD11a-mYFP CD8<sup>+</sup> T cell adhesion on ICAM-1-coated plates (**d**) and the area and spreading speed calculated from zones including all TIRF signals for each cell (**e**); scale bar, 20 μm. Each dot represents one cell ( $n = 3$ ). Bars indicate the means. **f**, Naive and activated CD8<sup>+</sup> T cell migration on ICAM-1- or ICAM-1 + CXCL12-coated surfaces ( $n = 3$  mice;  $n = 21$ –42 individual cells per mouse). **g**, Schematic illustrating the regulation of LFA-1 endocytic recycling via βII-spectrin or ST3GAL1 expression (created with BioRender.com). **h**, βII-Spectrin

(GFP<sup>+</sup>) expression in T cells isolated from *GFP-Rosa<sup>βII-spectrin</sup>* mice (T<sub>βII-spectrin</sub> cells) after *in vitro* treatment with TAT-Cre recombinase. **i**, Cross-section images in the middle of hHER2 CAR T cell (WT and T<sub>βII-spectrin</sub> cells)-endothelial cell (EC; bEND.3 cells) contacts by transmission electron microscopy. Black arrows indicate LFA-1 stainings at the cell–cell contacts; scale bars, 2 μm and 0.1 μm. **j**, The ratio of the TIRF microscopy signal from LFA-1 accumulation of hHER2 CAR T cells (WT and T<sub>βII-spectrin</sub> cells) at sites of contact with the ICAM-1-coated surface ( $n = 3$ ). **k**, Flow cytometry analysis of MAL-II binding to naive and activated CD8<sup>+</sup> T cells (WT, T<sub>βII-spectrin</sub> and T<sub>βII-spectrin</sub> + *St3gall1*-shRNA-treated cells;  $n = 3$ ). Representative images or data were collected from three independent experiments (**a**, **b**, **f** and **h**) or two independent experiments (**i**). Results are shown as the mean ± s.e.m. (**c** and **f**) and MFI ± s.e.m. (**k**). Statistical analyses were performed by ordinary two-way ANOVA (**c**) or two-sided, unpaired Student's *t*-test (**e**, **f**, **j** and **k**).

and  $\beta$ II-spectrin-overexpressing hHER2 CAR T cells was further confirmed quantitatively by measuring the cell surface topography of LFA-1 with TIRF:epi ratio signals (Fig. 4j). Notably,  $\beta$ II-spectrin overexpression was sufficient to decrease MAL-II binding on CAR T cell surfaces and the combination of  $\beta$ II-spectrin overexpression and *St3gal1* deletion further reduced cell surface sialylated glycan activity (Fig. 4k).

Interestingly, we observed chemokine-independent migration only in activated CD8<sup>+</sup> T cells but not in CD4<sup>+</sup> T cells (Extended Data Fig. 7e). Unlike CD8<sup>+</sup> T cells, adoptively transferred in vitro activated CD4<sup>+</sup> T cells did not accumulate in the lung (Extended Data Fig. 7f). ST3GAL1 expression was low in naive CD4<sup>+</sup> and CD8<sup>+</sup> T cells and similarly upregulated in both cell types after in vitro activation (Extended Data Fig. 7g).  $\beta$ II-Spectrin was highly expressed in both naive CD4<sup>+</sup>





and CD8<sup>+</sup> T cells (Extended Data Fig. 7g). However, unlike in activated CD8<sup>+</sup> T cells, the expression level of βII-spectrin remained constant after CD4<sup>+</sup> T cell activation (Extended Data Fig. 7g). These results

suggest that differential chemokine reliance for T cell migration may be linked to distinct βII-spectrin expression, leading to altered LFA-1 regulation after in vitro activation. Intriguingly, memory CD8<sup>+</sup>

### Fig. 5 | $\beta$ II-spectrin expression predicts response to CAR T cell therapy.

**a**, Schematic showing the assessment of tissue homing of  $T_{\beta\text{II-spectrin}}$  (green) and  $T_{\text{control}}$  (red) cells transfected with hHER2 CAR in hHER2 transgenic mice bearing B16-hHER2 tumors (created with BioRender.com). **b**,  $T_{\beta\text{II-spectrin}}$  (green) and  $T_{\text{control}}$  (red) hHER2 CAR T cells were cotransferred (1:1 mix), and the fold change in the homing index was analyzed at each time point ( $n = 5$  mice per condition). **c**, Representative deep 3D imaging (1-mm thick) of CAR T cell accumulation in a cleared mouse lung 72 h after intravenous injection; blue, blood vessels (CD31); green, CAR  $T_{\beta\text{II-spectrin}}$  cells; red, CAR  $T_{\text{control}}$  cells; scale bars, 100  $\mu\text{m}$ . **d**, Tumor growth and final tumor size from hHER2 transgenic mice bearing B16-hHER2 tumors infused with  $T_{\beta\text{II-spectrin}}$  and  $T_{\text{control}}$  cells transfected with hHER2 CAR ( $n = 10$  mice per group). **e**, Mouse survival curves up to 50 d after tumor inoculations. **f**, Frequency of CAR T cells over total lymphocytes in B16-hHER2 tumors, lungs or dLNs as measured by flow cytometry on day 22 ( $n = 4$ ). **g**,  $\beta$ II-Spectrin western blotting of CAR T cell infusion products obtained from 23 individuals with B cell lymphoma who showed complete recovery (CR), partial recovery (PR) or progressive disease (PD). Representative male and female samples from each group are shown. **h**, Quantification of total  $\beta$ II-spectrin protein expression in CAR T cell products from participants with CR, PR or PD as determined by western blotting. **i**, Correlation between  $\beta$ II-spectrin expression in CAR T cell products and neurotoxic effects and CRS. Pearson correlation calculations were performed for linear correlations. **j**, Luminex assay of the proinflammatory cytokines IFN $\gamma$ , IL-6 and IL-1 $\beta$  in serum before (day -5) and after (day 2) CAR T cell infusion. The data represent the mean  $\pm$  s.e.m. (**b**, **d**, **f** and **h**). Statistical analyses were performed by ordinary two-way ANOVA (**d**), two-sided, unpaired Student's *t*-test (**b**, **d** and **h**) or two-sided log-rank Mantel-Cox test (**e**). Whiskers represent maximum and minimum values (**d**, **f** and **h**).

T cells showed a similar expression level of  $\beta$ II-spectrin as naive T cells (Extended Data Fig. 7h).

### Expression of $\beta$ II-spectrin improves tumor-specific homing of CAR T cells

We then performed in vivo competitive homing assays with T cells isolated from *GFP-Rosa $^{\beta\text{II-spectrin}}$*  mice ( $T_{\beta\text{II-spectrin}}$ ) and *Rosa $^{d\text{Tmato}}$*  ( $T_{\text{control}}$ ) mice. TAT-Cre-treated  $T_{\beta\text{II-spectrin}}$  (green) and  $T_{\text{control}}$  (red) cells were transfected with hHER2 CAR and mixed 1:1 and then intravenously injected into hHER2 transgenic mice bearing B16-hHER2 tumors (Fig. 5a). During the early phase of adoptive transfer, a significantly lower number of CAR  $T_{\beta\text{II-spectrin}}$  cells were recruited to the lung than CAR  $T_{\text{control}}$  cells (Fig. 5b). Instead, CAR  $T_{\beta\text{II-spectrin}}$  cells showed a greater capacity to migrate to tumors, leading to a dramatic increase in intratumoral accumulation compared to CAR  $T_{\text{control}}$  cells (Fig. 5b,c). Compared to control hHER2 tumor-bearing mice into which CAR  $T_{\text{control}}$  cells were adoptively transferred, tumor-bearing mice in which CAR  $T_{\beta\text{II-spectrin}}$  cells were adoptively transferred showed pronounced tumor regression and a significant improvement in long-term survival (Fig. 5d,e). Differences in tumor size were apparent as early as day 14 after adoptive T cell transfer and were associated with a marked increase in intratumoral and intralymph nodal CAR  $T_{\beta\text{II-spectrin}}$  cell infiltration (Fig. 5f). These results suggest that the expression of  $\beta$ II-spectrin in CAR T cells promotes their recruitment to target tumor sites and suppresses tumor growth.

### $\beta$ II-Spectrin expression predicts response to CAR T cell therapy

Our data suggest that dramatic downregulation of  $\beta$ II-spectrin is closely associated with nonspecific sequestration of the adoptively transferred T cells and may be coincident with reduced therapeutic outcomes and/or a delayed overall response and an increase in cytokine signatures of systemic toxicity. To test this hypothesis in CAR T cell therapy, we collected human CAR T cells and performed serial blood collections from individuals on CD19 CAR T cell therapy (axicabtagene ciloleucel) before (day -5) and after treatment (day 2 after the injection of CAR T cells; Fig. 1a and Supplementary Table 3). At the 100-d follow-up with micro-PET/CT, 10 participants had progressive disease (42%) and 14 showed partial response or complete response (58%). Western blotting of the CD19 CAR T cells revealed a significantly higher expression level of  $\beta$ II-spectrin in CAR T cells within the infusion products of participants who had achieved partial response or complete response (Fig. 5g,h).

The two most commonly observed adverse events associated with CD19 CAR T cell treatment are CRS and neurotoxic effects<sup>40</sup>. Overall, the CRS of any grade occurred in 22 participants (92%). Grade 1–2 neurotoxic effects were observed in four individuals (17%), grade 3 was observed in seven (29%), and grade 4–5 was observed in four (17%). We found that there were similar inverse trends in the CAR T cell  $\beta$ II-spectrin expression levels versus the severity grades of CRS and neurotoxic effects ( $P = 0.05$ ; Fig. 5i), suggesting that  $\beta$ II-spectrin expression may be an independent predictor of severe toxic effects.

We then explored whether the inverse correlation between  $\beta$ II-spectrin expression and severe toxic effects can be explained by serum cytokine levels. Interestingly, participants with progressive disease (with a significantly lower expression level of  $\beta$ II-spectrin in their CAR T cell products; Fig. 5h) showed a greater upregulation of serum cytokine expression before (day -5) than after (day 2) CAR T cell infusion (Fig. 5j), indicating that systemic inflammatory cytokine production may be dependent on  $\beta$ II-spectrin expression.

### Discussion

Our study supports a paradigm suggesting that the ability of in vitro activated therapeutic T cells to home to target tissues may not be completely dictated by local chemokine signals but is additionally controlled by an important cell-intrinsic program that is acquired by T cells during the ex vivo manufacturing process. This paradigm explains why adoptively transferred T cells predominantly localize to nonspecific tissue sites. We have shown that the ST3GAL1- $\beta$ II-spectrin axis controls tissue-specific migration of intravenously transferred in vitro activated therapeutic T cells and that suppression of ST3GAL1 function and/or restoration of  $\beta$ II-spectrin expression improves chemokine-dependent and tissue-specific migration of therapeutic T cells, including CAR T cells, while reducing their nonspecific sequestration in non-inflamed tissues.

In an early clinical trial, an individual with metastatic colorectal cancer who received an infusion of HER2 CAR T cells experienced acute respiratory distress and pulmonary edema and subsequently died<sup>41</sup>. The toxicity detected in this individual was mainly caused by acute pulmonary sequestration of the intravenously administered HER2 CAR T cells and massive release of inflammatory cytokines after interaction with the HER2 antigen expressed in the normal lung endothelium and epithelial cells. Therefore, it is tempting to speculate that the prolonged and strong interaction of highly activated engineered T cells with the target antigen in non-tumor-bearing tissues may be a driving factor for CRS in other CAR T cell therapies.

$\beta$ II-Spectrin generally forms a heterodimer with  $\alpha$ -spectrins. Interestingly,  $\alpha$ -spectrins contain a highly conserved Src homology 3 domain (SH3), suggesting that it may mediate intracellular signals by recruiting or activating downstream molecules through the SH3 domain. We show that  $\beta$ II-spectrin restoration in activated CD8 $^+$  T cells decreases spontaneous cell migration, while this overexpression preserves chemokine-dependent migration. We further confirmed that  $\beta$ II-spectrin expression had no effect on CD8 $^+$  T cell activation and effector functions both in vitro and in vivo. How LFA-1 directly interacts with  $\beta$ II-spectrin is unknown and will be an important topic for future research. Spectrins can bind F-actin and may interact with integrins through adaptor proteins, such as talin and kindlin, or through other proteins involved in the association of F-actin with the membrane<sup>42,43</sup>.

As seen with integrin-independent migration in 3D tissue environments, it is also possible that chemokine-insensitive migration can simply be another tool that T cells use to facilitate migration under

conditions that are restrictive to traditional migration mechanisms. Random migration in the inflamed tissue may increase the likelihood that cells encounter chemokine signals that will direct them to the site of infection to elicit effector functions. Shulman et al.<sup>27</sup> have shown that transmigration may be facilitated through intracellular chemokine stores that require direct T cell interaction. Therefore, T cell crawling along endothelial cells in the absence of extracellular chemokine signaling may facilitate discovery of these intracellular stores of chemokines to induce transmigration. It is important to note that chemokine-insensitive migration does not mean that cells will not respond to chemokine stimulation. Instead, this should be considered a mechanism through which cells can find the general site of infection, while chemokine signals play a key role in ensuring precise localization.

## Online content

Any methods, additional references, Nature Portfolio reporting summaries, source data, extended data, supplementary information, acknowledgements, peer review information; details of author contributions and competing interests; and statements of data and code availability are available at <https://doi.org/10.1038/s41590-023-01498-x>.

## References

1. Aghajanian, H., Rurik, J. G. & Epstein, J. A. CAR-based therapies: opportunities for immuno-medicine beyond cancer. *Nat. Metab.* **4**, 163–169 (2022).
2. Lizee, G. et al. Harnessing the power of the immune system to target cancer. *Annu. Rev. Med.* **64**, 71–90 (2013).
3. Bobisse, S. et al. Reprogramming T lymphocytes for melanoma adoptive immunotherapy by T-cell receptor gene transfer with lentiviral vectors. *Cancer Res.* **69**, 9385–9394 (2009).
4. Junghans, R. P. The challenges of solid tumor for designer CAR-T therapies: a 25-year perspective. *Cancer Gene Ther.* **24**, 89–99 (2017).
5. Hernandez-Lopez, A., Tellez-Gonzalez, M. A., Mondragon-Teran, P. & Meneses-Acosta, A. Chimeric antigen receptor-T cells: a pharmaceutical scope. *Front. Pharm.* **12**, 720692 (2021).
6. Fowell, D. J. & Kim, M. The spatio-temporal control of effector T cell migration. *Nat. Rev. Immunol.* **21**, 582–596 (2021).
7. Mueller, K. T. et al. Cellular kinetics of CTL019 in relapsed/refractory B-cell acute lymphoblastic leukemia and chronic lymphocytic leukemia. *Blood* **130**, 2317–2325 (2017).
8. Lee, D. W. et al. T cells expressing CD19 chimeric antigen receptors for acute lymphoblastic leukaemia in children and young adults: a phase 1 dose-escalation trial. *Lancet* **385**, 517–528 (2015).
9. Morgan, R. A. et al. Case report of a serious adverse event following the administration of T cells transduced with a chimeric antigen receptor recognizing ERBB2. *Mol. Ther.* **18**, 843–851 (2010).
10. Finkle, D. et al. HER2-targeted therapy reduces incidence and progression of midlife mammary tumors in female murine mammary tumor virus huHER2-transgenic mice. *Clin. Cancer Res.* **10**, 2499–2511 (2004).
11. Amitrano, A. M. et al. Optical control of CD8<sup>+</sup> T cell metabolism and effector functions. *Front. Immunol.* **12**, 666231 (2021).
12. Paley, M. A. et al. Progenitor and terminal subsets of CD8<sup>+</sup> T cells cooperate to contain chronic viral infection. *Science* **338**, 1220–1225 (2012).
13. You, R. et al. Active surveillance characterizes human intratumoral T cell exhaustion. *J. Clin. Investig.* **131**, e144353 (2021).
14. Donnadieu, E., Dupre, L., Pinho, L. G. & Cotta-de-Almeida, V. Surmounting the obstacles that impede effective CAR T cell trafficking to solid tumors. *J. Leukoc. Biol.* **108**, 1067–1079 (2020).
15. Platt, R. J. et al. CRISPR-Cas9 knockin mice for genome editing and cancer modeling. *Cell* **159**, 440–455 (2014).
16. Zimmermann, M. et al. CRISPR screens identify genomic ribonucleotides as a source of PARP-trapping lesions. *Nature* **559**, 285–289 (2018).
17. Hobbs, S. J. & Nolz, J. C. Regulation of T cell trafficking by enzymatic synthesis of O-glycans. *Front. Immunol.* **8**, 600 (2017).
18. Pietrobono, S. et al. ST3GAL1 is a target of the SOX2-GLI1 transcriptional complex and promotes melanoma metastasis through AXL. *Nat. Commun.* **11**, 5865 (2020).
19. Priatel, J. J. et al. The ST3Gal-I sialyltransferase controls CD8<sup>+</sup> T lymphocyte homeostasis by modulating O-glycan biosynthesis. *Immunity* **12**, 273–283 (2000).
20. Giovannone, N. et al. Human B cell differentiation is characterized by progressive remodeling of O-linked glycans. *Front. Immunol.* **9**, 2857 (2018).
21. Chen, S. et al. Increased SPC24 in prostatic diseases and diagnostic value of SPC24 and its interacting partners in prostate cancer. *Exp. Ther. Med.* **22**, 923 (2021).
22. Geisler, C. & Jarvis, D. L. Effective glycoanalysis with *Maackia amurensis* lectins requires a clear understanding of their binding specificities. *Glycobiology* **21**, 988–993 (2011).
23. Sen, M. & Springer, T. A. Leukocyte integrin  $\alpha_1\beta_2$  headpiece structures: the  $\alpha 1$  domain, the pocket for the internal ligand, and concerted movements of its loops. *Proc. Natl. Acad. Sci. USA* **113**, 2940–2945 (2016).
24. Walling, B. L. & Kim, M. LFA-1 in T cell migration and differentiation. *Front. Immunol.* **9**, 952 (2018).
25. Galkina, E. et al. Preferential migration of effector CD8<sup>+</sup> T cells into the interstitium of the normal lung. *J. Clin. Investig.* **115**, 3473–3483 (2005).
26. Walch, J. M. et al. Cognate antigen directs CD8<sup>+</sup> T cell migration to vascularized transplants. *J. Clin. Investig.* **123**, 2663–2671 (2013).
27. Shulman, Z. et al. Transendothelial migration of lymphocytes mediated by intraendothelial vesicle stores rather than by extracellular chemokine depots. *Nat. Immunol.* **13**, 67–76 (2011).
28. Cyster, J. G. & Goodnow, C. C. Pertussis toxin inhibits migration of B and T lymphocytes into splenic white pulp cords. *J. Exp. Med.* **182**, 581–586 (1995).
29. Surve, C. R., Lehmann, D. & Smrcka, A. V. A chemical biology approach demonstrates G protein  $\beta$  subunits are sufficient to mediate directional neutrophil chemotaxis. *J. Biol. Chem.* **289**, 17791–17801 (2014).
30. Kim, M., Carman, C. V. & Springer, T. A. Bidirectional transmembrane signaling by cytoplasmic domain separation in integrins. *Science* **301**, 1720–1725 (2003).
31. Kim, M., Carman, C. V., Yang, W., Salas, A. & Springer, T. A. The primacy of affinity over clustering in regulation of adhesiveness of the integrin  $\alpha_1\beta_2$ . *J. Cell Biol.* **167**, 1241–1253 (2004).
32. Feng, Y. et al. Exo1: a new chemical inhibitor of the exocytic pathway. *Proc. Natl. Acad. Sci. USA* **100**, 6469–6474 (2003).
33. Nishikimi, A. et al. Rab13 acts downstream of the kinase Mst1 to deliver the integrin LFA-1 to the cell surface for lymphocyte trafficking. *Sci. Signal* **7**, ra72 (2014).
34. De Franceschi, N., Hamidi, H., Alanko, J., Sahgal, P. & Ivaska, J. Integrin traffic—the update. *J. Cell Sci.* **128**, 839–852 (2015).
35. Meissner, J. M. et al.  $\alpha II$ -Spectrin in T cells is involved in the regulation of cell–cell contact leading to immunological synapse formation? *PLoS ONE* **12**, e0189545 (2017).
36. Capace, T. et al. A novel intracellular pool of LFA-1 is critical for asymmetric CD8<sup>+</sup> T cell activation and differentiation. *J. Cell Biol.* **216**, 3817–3829 (2017).
37. Thomsen, P., Roepstorff, K., Stahlhut, M. & van Deurs, B. Caveolae are highly immobile plasma membrane microdomains, which are not involved in constitutive endocytic trafficking. *Mol. Biol. Cell* **13**, 238–250 (2002).

38. Fritzsche, M. & Charras, G. Dissecting protein reaction dynamics in living cells by fluorescence recovery after photobleaching. *Nat. Protoc.* **10**, 660–680 (2015).
39. Lingel, H. et al. CTLA-4-mediated posttranslational modifications direct cytotoxic T-lymphocyte differentiation. *Cell Death Differ.* **24**, 1739–1749 (2017).
40. Park, J. H. et al. Long-term follow-up of CD19 CAR therapy in acute lymphoblastic leukemia. *N. Engl. J. Med.* **378**, 449–459 (2018).
41. Heslop, H. E. Safer CARS. *Mol. Ther.* **18**, 661–662 (2010).
42. Beaty, B. T. et al. Talin regulates moesin-NHE-1 recruitment to invadopodia and promotes mammary tumor metastasis. *J. Cell Biol.* **205**, 737–751 (2014).
43. Medina, E. et al. Crumbs interacts with moesin and  $\beta_{\text{Heavy}}$ -spectrin in the apical membrane skeleton of *Drosophila*. *J. Cell Biol.* **158**, 941–951 (2002).
44. Gossez, M. et al. Evaluation of a novel automated volumetric flow cytometer for absolute CD4 $^{+}$  T lymphocyte quantitation. *Cytometry B* **92**, 456–464 (2017).

**Publisher's note** Springer Nature remains neutral with regard to jurisdictional claims in published maps and institutional affiliations.

Springer Nature or its licensor (e.g. a society or other partner) holds exclusive rights to this article under a publishing agreement with the author(s) or other rightsholder(s); author self-archiving of the accepted manuscript version of this article is solely governed by the terms of such publishing agreement and applicable law.

© The Author(s), under exclusive licence to Springer Nature America, Inc. 2023

## Methods

### Antibodies and reagents

OneComp eBeads and PE-anti-human IgG Fc were purchased from eBioscience. Anti-mouse CD16/CD32 Fc blocker, antibodies to  $\alpha$ -spectrin and  $\beta$ II-spectrin for western blotting and a BD Cytofix/Cytoperm fixation/permeabilization kit were purchased from BD Biosciences. Antibodies to LFA-1-APC (H155-78), CD45.1-FITC (A20), CD45.2-BV711 (104), CD8-PE/Cy7 (53-6.7), CD8-AF594 (53-6.7), CD11a-AF647 (M17/4), CD11a-AF488 (M17/4), CD31-PB (390), CD31-AF647 (390), IFN $\gamma$ -BV421 (XMG1.2), TNF-BV421 (MP6-XT22), TIM-3-BV605 (RMT3-23), PD-1-BV421 (29F.1A12), granzyme B-APC (QA18A28), Ki67-APC (16A8), CD11c-BV711 (N418) and I-A/I-E-BV711 (M5/114.15.2) and anti-mouse IgG-AF647, anti-rat IgG-AF647, anti-CD11a (M17/4 or TS2/4), anti-CD18 (CBR LFA-1/2 or M18/2), anti-CD49d (R1-2), anti-MyH9 (Poly19098) and 7-AAD viability staining solution (420403) were purchased from BioLegend. PNGase F and  $\alpha$ -2,3-neuraminidase were purchased from New England Biolabs. Recombinant human IL-2, recombinant mouse IL-7 and IL-15 were obtained from PeproTech. *M. amurensis* lectin (MAA/MAL-II)-Cy5 and *M. amurensis* lectin (MAA/MAL-II)-Separopore 4B were purchased from glycoMatrix. TAT-Cre recombinase, PTx and ExtrAvidin-Peroxidase were purchased from Sigma. Biotinylated goat anti-rat IgG (H + L) was purchased from Vector Lab. Recombinant human ERBB2/HER2 Fc chimeric protein and human ERBB2/HER2-Alexa Fluor 594 were obtained from R&D Systems. Anti-ST3GAL1 was obtained from LS Bio. Anti- $\beta$ II-spectrin (F11) for western blotting and *St3gal1*-short hairpin RNA (*St3gal1*-shRNA) plasmid were purchased from Santa Cruz Biotechnology. Anti- $\beta$ -actin, anti-HER2/ERBB2 and horseradish peroxidase-conjugated anti-rabbit or anti-mouse were purchased from Cell Signaling Technology. RetroNectin was purchased from Takara Bio. Anti-CD18 was obtained from Abcam. FTY720 was purchased from CaymanChem. Exo1 was purchased from Tocris. Lipofectamine 2000, a CellTrace Far-Red cell proliferation kit, a CellTrace CFSE cell proliferation kit and DyLight/650-anti-human IgG Fc were obtained from Invitrogen.

### Mice

C57BL/6J, Rosa26-Cas9 knock-in, OT-I TCR, OT-II TCR, *Lfa-1*-KO, B6-GFP and Rosa<sup>tdTomato</sup> mice were purchased from the Jackson Laboratory. CD11a-mYFP, CD18-mCFP and GFP-Rosa <sup>$\beta$ II-spectrin</sup> mice were generated at the Gene Targeting and Transgenic Core facility at the University of Rochester using similar gene-targeting techniques previously used in our laboratory<sup>30,36</sup>. LFA-1 heterozygous mice were generated through breeding *Lfa-1*-KO mice (Jackson Laboratory) with CD11a-mYFP mice. Mice exhibited a 49–57% decrease in CD11a expression. hHER2 transgenic mice were obtained from Genentech<sup>10</sup>. Genotyping for each strain was performed according to the corresponding reference. All mice were further backcrossed with C57BL/6J mice for at least more than 12 generations. Seven- to 10-week-old female or male mice were used in this study. The mice were maintained under 12-h light/12-h dark cycles at 18–26 °C and 30–70% humidity. Mice were fed with rodent diet 5010 (LabDiet) and given reverse osmosis-filtered water (HYDROPAC). All animal experiments were performed in the Association for Assessment and Accreditation of Laboratory Animal Care International-accredited, specific pathogen-free facilities in the Division of Laboratory Animal Resources of the University of Rochester Medical Center. All animal experiments were approved by the University Committee on Animal Resources at the University of Rochester. Mice were killed at the indicated time points or when the geometric mean of tumor burden was  $\geq 2.0 \text{ cm}^3$ .

### Cell culture

B16-OVA and B16-hHER2 cells were cultured in DMEM supplemented with 10% fetal bovine serum (FBS), 1% penicillin-streptomycin and 1 mg ml<sup>-1</sup> G418 (Gibco). bEND.3 cells (ATCC) were cultured in DMEM

supplemented with 10% FBS and 1% penicillin-streptomycin, and 293T Phoenix cells were cultured in DMEM supplemented with 10% FBS, 1% penicillin-streptomycin, 20 mM HEPES (Gibco), 1% MEM non-essential amino acids (Gibco) and 50  $\mu\text{M}$   $\beta$ -mercaptoethanol (Sigma-Aldrich). Platinum-E cells were cultured in DMEM supplemented with 10% FBS, 1% penicillin-streptomycin, 1  $\mu\text{g ml}^{-1}$  puromycin and 10  $\mu\text{g ml}^{-1}$  blasticidin S-HCl. Purified mouse and human CD8<sup>+</sup> T cells were cultured in RPMI 1640 supplemented with 10% FBS, 1% antibiotic-antimycotic (Gibco), 2 mM L-glutamine (Gibco), 20 mM HEPES (Gibco), 1% MEM non-essential amino acids (Gibco), 50  $\mu\text{M}$   $\beta$ -mercaptoethanol (Sigma-Aldrich) and 80 U ml<sup>-1</sup> IL-2. All cells were maintained at 37 °C in 5% CO<sub>2</sub>. For the B16-hHER2 stable cell line, B16F10 mouse melanoma cells (ATCC) were transfected with hHER2 pcDNA3.1 mammalian expression plasmid (Addgene, 16257) using Lipofectamine 2000 according to the manufacturer's protocol. Antibiotic selection (G418, 1 mg ml<sup>-1</sup>) was added to the medium 24 h after transfection. Cells were stained with anti-hHER2 and sorted for the top 5% of HER2 expressers. Sorted cells were plated in 96-well plates at 1 cell per well to generate single-cell clones. When thawed, stable cells were cultured in the presence of G418 and used within 2 weeks.

### T cell preparation and CAR T cell generation

CD4<sup>+</sup> or CD8<sup>+</sup> T cells were prepared from negative selection via Dynabeads (Invitrogen) or a CD8a<sup>+</sup> T cell isolation kit (Miltenyi) with 99% purity. Purified T cells were activated with plate-bound 6  $\mu\text{g ml}^{-1}$  anti-CD3 $\epsilon$  and 1.6  $\mu\text{g ml}^{-1}$  anti-CD28 for 1 d and cultured with IL-2. Human T cells were purified from peripheral blood of healthy donors or individuals with cancer treated with CAR T cell therapy by using the EasySep Direct human T cell isolation kit (StemCell). CD8<sup>+</sup> T cells isolated from healthy donors were activated with Dynabeads Human T-Activator CD3/CD28 (Gibco) for 2 d, followed by incubation with IL-2. For CAR T studies, activated mouse CD8<sup>+</sup> T cells were transfected with trastuzumab (4D5; anti-HER2)-based CAR. CAR sequence was first cloned into the pMSCV vector (631461, Clontech). Retrovirus was generated using the Platinum-E packaging cell line. Platinum-E cells were plated at 0.8  $\times 10^6$  cells per well in a six-well plate. The following day, Platinum-E cells were transfected with hHER2 CAR pMSCV vector and pCI-Eco packaging vector using Lipofectamine 2000 (Invitrogen) according to the manufacturer's protocol. Medium was swapped 6 h after transfection. Retroviral-containing supernatants were collected 48 and 72 h after transfection. For T cell transduction, 1  $\times 10^6$  activated CD8<sup>+</sup> T cells were plated on RetroNectin-coated (10  $\mu\text{g ml}^{-1}$ ; Takara) 12-well plates with retrovirus-containing supernatants supplemented with 80 U ml<sup>-1</sup> IL-2 and centrifuged twice at 48 and 72 h after transfection at 2,500 r.p.m. T cells were then detached from RetroNectin-coated plates at least 24 h after transduction and analyzed for hHER2 CAR expression. GFP-Rosa <sup>$\beta$ II-spectrin</sup> mouse-derived CD8<sup>+</sup> T cells were pretreated with TAT-Cre recombinase (4.4  $\mu\text{M}$ ; Sigma) for 30 min to induce  $\beta$ II-spectrin expression and were transduced with hHER2 CAR. To knockdown *St3gal1* in GFP-Rosa <sup>$\beta$ II-spectrin</sup> mouse-derived CD8<sup>+</sup> T cells, T cells were transfected with *St3gal1*-shRNA plasmid (Santa Cruz) after treatment with TAT-Cre recombinase.

### T cell electroporation

Six to 7 h before transfection, CD8<sup>+</sup> T cells were washed with lymphocyte separation medium and allowed to rest in complete medium; 2  $\times 10^6$  cells were suspended in P3 primary cell transfection medium (Lonza) and mixed with *Rab13* siRNA (Thermo). For  $\beta$ II-spectrin,  $\beta$ II-spectrin-hemagglutinin DNA was purchased from Addgene (plasmid 31070) and mixed with monomeric RFP plasmids. T cell electroporation was performed using an Amaxa 4D-Nucleofector kit (Lonza) with the DN-100 protocol, following the manufacturer's instructions. Cells were incubated in mouse T cell Nucleofector medium + IL-2 for 6 h after transfection before being transferred to complete medium + IL-2. Cells were analyzed 24 h after transfection.

## In vivo studies

B16-hHER2 cells ( $2 \times 10^5$ ) in 10  $\mu\text{l}$  of PBS were intradermally injected into one ear pinna of recipient hHER2 transgenic mice. For adoptive cell transfer experiments, CAR T cells were pretreated with anti-CD49d (200  $\mu\text{g}$ ; R1-2, Biolegend), anti-CD11a (200  $\mu\text{g}$ ; M17/4, Biolegend) or PTx (100 ng  $\text{ml}^{-1}$ ; Sigma) for 1 h or 6 h, respectively, before injection. Pretreated  $5 \times 10^6$  T cells were injected intravenously via the tail vein. Organs, including lungs, spleens and LNs, were extracted 4 h after injection and analyzed. For the egress assay,  $5 \times 10^6$  T cells were injected intravenously via the tail vein, and FTY720 (1 mg  $\text{kg}^{-1}$ ; Cayman Chem) was injected into the peritoneal cavity 24 and 48 h after injection of CAR T cells. Organs, including lungs, spleens, and LNs, were extracted 72 h after injection and analyzed.

For competitive homing assays, a 1:1 mix of  $5 \times 10^6$  CAR T cells stained with CFSE or Far-Red (Invitrogen) or expressing GFP or tdTomato were injected intravenously through the tail vein. Several organs were collected at specific times (4, 24, 48 or 72 h) after intravenous injection, and the distribution of cells was confirmed. The fold change of homing index was determined by  $(\text{CFSE}^{+\text{sample}}/\text{CFTR}^{+\text{sample}})/(\text{CFSE}^{+\text{input}}/\text{CFTR}^{+\text{input}})$  or  $(\text{GFP}^{+\text{sample}}/\text{tdTomato}^{+\text{sample}})/(\text{GFP}^{+\text{input}}/\text{tdTomato}^{+\text{input}})$ . For tumor growth analysis,  $5 \times 10^5$  B16-hHER2 cells were subcutaneously injected into a left hinge flank of recipient hHER2 transgenic mice. On day 7 after tumor inoculation,  $3 \times 10^6$  HER2 CAR T cells were injected intravenously via the tail vein. Tumor growth was monitored every 3 d. Tumor volume was calculated using the formula tumor volume = width $^2$  × length/2. On day 22, lungs, tumor dLNs, and tumor tissues were extracted and analyzed. As stipulated by the Institutional Animal Care and Use Committee, the survival experiment was performed by setting the point when the tumor size reached 2,000  $\text{mm}^3$  as the end point.

## T cell cytotoxicity assay

Target cells (B16-hHER2 cells or B16-OVA cells) were seeded in 24-well plates at  $1 \times 10^4$  cells per well, and effector cells (CAR T cells or Cas9-OT-I T cells) expressing GFP were added to the target cells at a 10:1 effector:target ratio. After 24 h of incubation at 37 °C, 7-AAD dye was treated for 10 min, and cells were analyzed on a BD LSR II flow cytometer.

## In vitro migration assays

Cells were treated for 6 h with PTx (100 ng  $\text{ml}^{-1}$ ) or gallein (10  $\mu\text{g} \text{ ml}^{-1}$ ) for 30 min before imaging. The PTx concentration used was determined based on previous publications<sup>27,28</sup> and from our studies where it blocks more than 80% of naive T cell migration. Cells were treated with apyrase for 30 min before imaging at the described concentrations and remained in solution throughout the imaging. Cells were treated with Exo1 (100  $\mu\text{m} \text{ ml}^{-1}$ ) for 30 min before imaging and remained in solution throughout imaging. Cell migration chambers (Millicell EZ slide eight-well glass (Millipore) and ΔT dishes (Bioparts)) were prepared by coating the glass bottom with 0.5 or 5  $\mu\text{g}$  of recombinant mouse ICAM-1 (Sino Biological), respectively, with or without the indicated chemokines (200 ng  $\text{ml}^{-1}$  unless otherwise noted). T cells were placed in L15 medium (Invitrogen) in the chamber at 37 °C, and video microscopy was conducted using a TE2000-U microscope (Nikon) coupled to a CoolSNAP HQ CCD camera with a  $\times 20/0.45$ -NA objective (CFI Plan Fluor ELWD DM, Nikon). For flow chamber assays, sticky-slide I<sup>0.6</sup> Luer (Ibidi) with 22 × 60 × 1 coverslips (Fisherbrand) were prepared with ICAM-1 in a stage-top incubator (Oko Labs) at 37 °C. Fresh L15 medium was pumped continuously through the slide at 1.0  $\text{dyn cm}^{-2}$ . Cells were allowed to adhere using a flow rate of >0.1  $\text{dyn cm}^{-2}$  before imaging. To study T cell migration on endothelial cells, bEND.3 cells were grown into a monolayer on I<sup>0.6</sup> Luer (Ibidi) with 22 × 60 × 1 coverslips (Fisherbrand) before the addition of T cells. WT or PTx-treated T cells were stained with CFSE or cell proliferation dye eFluor670 (eBioscience), respectively, and mixed at a 1:1 ratio. Mixed T cells ( $2.5 \times 10^5$ ) were

allowed to adhere using a flow rate of >0.1  $\text{dyn cm}^{-2}$  before imaging. Fresh L15 medium was then pumped continuously through the slide at 1.0  $\text{dyn cm}^{-2}$  for the remainder of the experiment. Migration analysis was performed in Velocity software (PerkinElmer). Transwell chamber assays were performed using a 5-μm pore, 24-well system (Corning). Filter membranes were coated with Protein A (20  $\mu\text{g} \text{ ml}^{-1}$ ) overnight at 4 °C before ICAM-1 coating (5  $\mu\text{g}$ ) for 2 h at room temperature. Lower chambers were filled with 500  $\mu\text{l}$  of complete medium supplemented with 200 ng  $\text{ml}^{-1}$  CXCL12 or 500 ng  $\text{ml}^{-1}$  CCL21, and  $1 \times 10^6$  cells were seeded into the upper wells and allowed to migrate for 3 h at 37 °C and 5% CO<sub>2</sub>. The lower wells were collected, supplemented with 5 × 10<sup>4</sup> counting beads (SphereTech) and counted using a flow cytometer. Each condition was run in triplicate. B16 spheroids were generated using the ‘hanging drop’ method. Briefly, 20 10- $\mu\text{l}$  droplets containing  $0.5 \times 10^4$  B16-hHER2-BFP tumor cells in complete DMEM were plated onto the lid of a 10-cm plate and inverted. Five milliliters of PBS was added to the 10-cm plate to prevent evaporation. After 96 h, the spheroids were collected by gentle pipetting and allowed to settle in a 1.4-ml Eppendorf tube, and excess medium was aspirated. hHER2 CAR T cells were stained with CellTrace Far-Red (Invitrogen) per the manufacturer’s protocol. In PTx treatments, the stained CAR T cells were pretreated with 1  $\mu\text{g} \text{ ml}^{-1}$  PTx (Sigma) for 6 h. Stained CAR T cells were resuspended in 50  $\mu\text{l}$  of complete RPMI and mixed with the tumor spheroids. Fifty microliters of Matrigel (Corning) was added to the stained CAR T cell/spheroid mixture and mixed thoroughly. The total volume (100  $\mu\text{l}$ ) was pipetted to the center of a ΔT dish (Bioparts) and incubated at 37 °C and 5% CO<sub>2</sub> for 30 min to allow the gel to polymerize into a 3D matrix. Once solidified, 1 ml of Leibovitz’s L15 medium supplemented with 2 mg  $\text{ml}^{-1}$  glucose was added to the dish, and live-imaging time-lapse microscopy was performed. Video microscopy was conducted in a 37 °C chamber. Brightfield and fluorescent images were acquired every 60 s for up to 24 h.

## RT-qPCR

For gene expression analysis of mouse or human CD8<sup>+</sup> T cells by RT-qPCR, cells were lysed in RLT buffer, and RNA was isolated with an RNeasy mini isolation kit (Qiagen), according to the manufacturer’s instructions. After RNA concentration and purity were checked using a NanoDrop, 100 ng of RNA per reaction was subsequently converted to cDNA using the SuperScript VILO cDNA synthesis kit (Invitrogen). Samples were assayed using SsoAdvanced Universal SYBR Green Supermix (Bio-Rad), and kinetic PCR was performed on a CFX Connect real-time PCR detection system (Bio-Rad). The indicated genes were analyzed by using the primers listed below. Data were normalized to the housekeeping gene valosin-containing protein (VCP) and hypoxanthine guanine phosphoribosyltransferase (HPRT). Relative transcript levels were analyzed using the cycling threshold ( $2^{-\Delta\Delta C_t}$ ) method. The following primers were used, with the format ‘target (forward primer/reverse primer)’: *HuSt3gal1* (GCATTTCTTTCCCACAGC/CTAACCCAGGCCACCTCA), *HuSPC24* (GGGATTATGAGTGTGAGCCAGG/ACTCCAGAGGTAGTCGCTGATG), *HuVCP* (AGGATGATCCAGTGCTGAGAG/GGAATCTGAAGCTGCCAAG), *MoSt3gal1* (GCAGACGTTGGGAGCCGGAC/GGCACGGGGACATAGGTGTGAG), *MoSPC24* (CAGTGGGATTATGAATGGCAGCC/GGTAGTCACTGATGAACCTCGC) and *MoHPRT* (GCTGGTAAAAGGACCTCT/CACAGGACTAGAACACCTGC).

## LFA-1 endocytosis assay

The protocol was modified from a previous study<sup>45</sup>. LFA-1 on the cell surface was labeled with anti-CD18 (CBRLFA-1/2; 10  $\mu\text{g} \text{ ml}^{-1}$ ), anti-CD11a (TS2/4; 10  $\mu\text{g} \text{ ml}^{-1}$ ) or anti-mouse CD18 (M18/2; 10  $\mu\text{g} \text{ ml}^{-1}$ ) for 30 min on ice. After washing with cold migration buffer, cells were treated with neuraminidase (200 ng  $\text{ml}^{-1}$ ) for 3 h at 37 °C. After washing with cold migration buffer, the cells were incubated with Alexa Fluor 647–anti-mouse IgG (Poly4053; 2  $\mu\text{g} \text{ ml}^{-1}$ ) or Alexa Fluor 647–anti-rat IgG (Poly4053; 2  $\mu\text{g} \text{ ml}^{-1}$ ) at 4 °C for 30 min and fixed immediately in 3%

paraformaldehyde (PFA). The MFI was acquired with a BD LSR II flow cytometer and analyzed with FlowJo.

### Flow cytometry and cell sorting

To detect CAR expression levels on T cells,  $1 \times 10^6$  CAR T cells were preincubated with anti-mouse CD16/CD32 Fc blocker (1 µg per 1 million cells in 100 µl; BD Bioscience) for 10 min at 4 °C and incubated with recombinant human ERBB2/HER2 Fc chimeric protein (R&D Systems) at 4 °C for 30 min. After washing, the cells were incubated with PE-anti-human IgG Fc (eBioscience) or DyLight/650-anti-human IgG Fc (Invitrogen) at 4 °C for 30 min. These stained cells were detected with a BD LSR II flow cytometer and analyzed with FlowJo. To detect MAL-II binding, cells were incubated with Cy5-MAL-II at 4 °C for 1 h in 1% bovine serum albumin (BSA)/PBS. For isolation of lymphocytes from organ tissues and tumors, mice were killed, and organs and tumors were extracted. Lungs, livers and tumors were minced into small fragments and digested with 1 mg ml<sup>-1</sup> collagenase D (Sigma) and 50 mg ml<sup>-1</sup> DNase (Roche) at 37 °C for 45 min and passed through a 40-µm cell strainer. Lymphocytes were isolated via Percoll gradient centrifugation. LNs and spleens were made into single-cell suspensions through 70-µm cell strainers. Red blood cells in single-cell suspensions were lysed with ACK lysis buffer (Thermo), washed with DPBS and prepared for antibody staining. For in vitro T cell staining, cells were restimulated with phorbol myristate acetate/ionomycin before staining. The obtained single cells were preincubated with anti-mouse CD16/CD32 Fc blocker (1 µg per 1 million cells in 100 µl; BD Bioscience) for 10 min at 4 °C and stained with the following antibodies at 4 °C for 1 h: TIM-3-BV605 (RMT3-23), PD-1-BV421 (29F.1A12), LFA-1-APC (H155-78), CD45.1-FITC (A20), CD45.2-BV711(104) and CD8-PE/Cy7 (53-6.7). Intracellular proteins or cytokines were stained with the following antibodies at 4 °C for 1 h after fixation and permeabilization with a BD Cytofix/Cytoperm fixation/permeabilization kit: IFNγ-BV421 (XMG1.2), TNF-BV421 (MP6-XT22), granzyme B-APC (QA18A28) and Ki67-APC (16A8). These stained cells were detected with a BD LSR II flow cytometer and analyzed with FlowJo. To analyze CAR T cells in the lungs, CAR T cells expressing GFP were sorted with a BD FACSaria II cell sorter from single-cell lymphocytes isolated from the mouse lungs.

### Glycosidase treatment

Twenty micrograms of CD8<sup>+</sup> T cell lysates were treated with 4 µl of α-2,3-neuraminidase (P0743L, New England Biolabs) and/or 2 µl of PNGase F (P0704L, New England Biolabs) at 37 °C overnight or for 2 h. Laemmli buffer (4×) was added, and the samples were denatured by heating at 95 °C. The samples were separated in 4–15% Mini-PROTEAN TGX precast protein gels (Bio-Rad), and western blots were performed as described below.

### Western blotting

Cells were lysed in RIPA buffer and separated in 4–15% Mini-PROTEAN TGX precast protein gels (Bio-Rad) by SDS-PAGE. After transferring the proteins to a nitrocellulose membrane, the membrane was blocked with 5% non-fat milk and 0.1% Tween 20 in TBS for 1 h. Blots were incubated with 1:500 anti-HER2 (Cell Signaling Technology), 1:500 anti-ST3GAL1 (LS Bio), 1:1,000 anti-SPC24 (Novus Bio), 1:1,000 anti-βII-spectrin (Santa Cruz), 1:500 anti-MyH9 (Biologend), 1:1,000 anti-αII-spectrin (BD Bioscience), 1:1,000 anti-CD18 (Abcam) and 1:5,000 anti-β-actin (Cell Signaling Technology) overnight at 4 °C. The membrane was then incubated with 1:3,000 horseradish peroxidase-conjugated anti-rabbit or anti-mouse (Cell Signaling Technology) for 1 h at room temperature. Images were obtained using a ChemiDoc imaging system (Bio-Rad).

### Immunoprecipitation

Immunoprecipitation was performed with the method we previously described<sup>46</sup>. Briefly, coverglasses were coated with 6 µg ml<sup>-1</sup> ICAM-1 or 10 µg ml<sup>-1</sup> poly-L-lysine. T cells were then incubated at 37 °C for

20 min on the coated coverglass in L15 medium (Invitrogen) containing 2 mg ml<sup>-1</sup> glucose or in 20 mM HEPES, 150 mM NaCl, 5 mM MgCl<sub>2</sub>, 1 mM EGTA and 2 mg ml<sup>-1</sup> glucose. Cell lysates were then precleared with 2 µg of mouse IgG isotype control and protein G agarose beads. Precleared lysates were incubated with protein G agarose and TS2/4 or CBRLFA-1/2 antibody. For immunoprecipitations with MAL-II, 30 µl of MAL-II agarose beads was mixed with 50 µg of cell lysates and incubated overnight at 4 °C on a rotator. The samples were washed with immunoprecipitation buffer and eluted by boiling in 2× Laemmli sample buffer. Equal volumes of immunoprecipitated samples were separated on 4–15% gradient gels (Bio-Rad) and stained with a SilverQuest silver staining kit (Invitrogen) or SimplyBlue SafeStain (Invitrogen) or were subjected to western blotting.

### LC-MS/MS

Purified CD18 was excised from Coomassie-stained gels and in-gel digested by trypsin. The digested peptides were extracted by gradient acetonitrile (ACN) with 0.1% trifluoroacetic acid (TFA) from 10 to 100% ACN. The extracted peptides were pooled and dried by speedvac. The peptides were then desalted using a Sep-Pak tC18 1 cc Vac cartridge (WAT054960). In brief, the columns were preequilibrated using 1 ml of 100% ACN and washed with 0.1% TFA twice. The digested peptides were added to 200 µl with 0.1% TFA, loaded into the columns and washed with 1 ml of 0.1% TFA twice, followed by 200 µl of 0.5% acetic acid. The digested peptides were eluted using 75% ACN/0.5% acetic acid. The eluted peptides were dried in a speedvac and dissolved in 0.1% formic acid for nanoLC-MS/MS using an Orbitrap Fusion mass spectrometer (Thermo Scientific) equipped with a nanoelectrospray ion source (New Objective) and an UltiMate 3,000 RSLCnano system pump (Thermo Scientific Dionex). PMI-Byonic was used for the MS/MS-based protein and glycosylation site identification<sup>47</sup>. Methionine oxidation was enabled as a variable modification. O-Glycopeptides were searched against 78 mammalian and 70 human databases.

### FRET and FRAP assays

FRET imaging was conducted with a dual-view image splitter (Photometrics) and a CFP/YFP dual-band filter set (Chroma) by the sensitized emission method as we previously described<sup>30</sup>. Data analysis was performed with the Autoquant imaging algorithm. FRET cells were resuspended in L15 medium with 2 mg ml<sup>-1</sup> glucose. Cells were placed in an uncoated ΔT dish and equilibrated for 10 min at 37 °C. Each image of CFP, YFP and DIC of each cell was acquired for 0.5 s with 2 × 2 binning through a ×60/1.49-NA oil immersion objective lens without an ND filter. For membrane versus cytosol experiments, regions of interest (ROIs) of the membrane and cytosol were selected for each cell. The FRET efficiency of each was then compared to generate a ratio of LFA-1 conformation between the two. FRAP was performed using an Olympus FV1000 laser-scanning confocal microscope housed at the University of Rochester Medical Center Confocal and Conventional Microscopy Core. Cells were imaged live using a ×60/1.4-NA oil immersion objective at 37 °C. FRAP was performed on βII-spectrin-expressing cells or WT control cells 24 h after transfection. Photobleaching was performed with the structured illumination microscopy scanner capabilities using the 488-nm laser line set to 100% power for 2 s, and images were collected every 3 s. FRAP analysis was performed using NIS Elements software. Two ROIs, one of the total cell membranes and one of the photobleached area, were collected following background correction. All fluorescent ROI values were reported as relative fluorescence units. Fluorescence values were normalized using the ratio of photobleached ROI to that of the control ROI. The recovery of fluorescence signals was calculated from the fluorescence of the bleached and non-bleached membrane areas during the time series.  $t_{1/2}$  values were calculated by fitting data to non-linear regression curves. The immobile fraction was calculated by subtracting the postbleached membrane fluorescence intensity from the prebleached intensity.

Mobile fraction ( $F_m$ ) =  $(I_E - I_0)/(I_t - I_0)$

Immobile fraction ( $F_i$ ) =  $1 - F_m$

$I_E$ : recovered fluorescence intensity

$I_0$ : postbleach fluorescence intensity

$I_t$ : prebleach fluorescence intensity

### TIRF microscopy

CD11a-mYFP CD8<sup>+</sup> T cells in L15 medium (Invitrogen) were allowed to settle on number 11/2 coverslips (Corning) coated with ICAM-1 (5 µg; Sino) with or without CXCL12 (200 ng ml<sup>-1</sup>; R&D Biological). hHER2 CAR T cells (WT and βII-spectrin) in L15 medium (Invitrogen) were allowed to settle on number 11/2 coverslips (Corning) coated with ICAM-1 (5 µg; Sino). TIRF was performed with the Andor Dragonfly TIRF microscopy module coupled to a Nikon Ti-E microscope equipped with a ×60/1.49-NA APO TIRF oil immersion objective and with images being captured by a Zyla 4.2 sCMOS camera (Andor). mYFP was excited with a fiber-coupled OBIS LX 488-nm wavelength solid-state laser (Coherent) line passed through a dichroic and 450/50-nm bandpass emission filter. All live-cell imaging was performed at 37 °C with 5% CO<sub>2</sub> with/without 20 µg of anti-CD11a (BD Biological) maintained by a stage-top incubator (Okolab) throughout the experiment. Images were acquired every second for 6–10 min. Image acquisition was performed using Fusion (Andor). All image processing was performed with MATLAB (Mathworks). For LFA-1 surface topography assays, cells were labeled with Alexa Flour 488 anti-mouse CD11a (clone I21/7, BioLegend). For controls, cells were labeled with Alexa Flour 488 in 1 ml of HBSS with 10 mM HEPES containing Alexa Flour 488 carboxyl acid and tetrafluorophenyl ester (component A from the protein labeling kit (Invitrogen)). Cells were spread onto ICAM-1- or BSA-coated coverslips. BSA-coated and uncoated coverslips served as controls. The cells were allowed to equilibrate for at least 20 min. A series of DIC, epi and TIRF images were acquired and saved for offline analysis. To avoid the potential artifacts in fluorescence due to changes in the cell shape as it interacted with the surface, TIRF signal was normalized by epi over a 2.0-µm diameter at the center of the contact zone. The normalized TIRF signal was calculated based on four ROIs for each image: the epi image at the center of the cell (Epi<sub>center</sub>), the epi image over the area where no cells were present for the epi background fluorescence measurement (Epi<sub>bkgd</sub>), TIRF image at the center of the cell (TIRF<sub>center</sub>) and TIRF over the area where no cells were present for the TIRF background fluorescence measurement (TIRF<sub>bkgd</sub>),

$$\text{TIRF : epi} = \frac{\text{TIRF}_{\text{center}} - \text{TIRF}_{\text{bkgd}}}{\text{epi}_{\text{center}} - \text{epi}_{\text{bkgd}}}.$$

### Electron microscopy

bEND.3 cells were seeded in cell migration chambers (Millicell EZ slide eight-well glass, Millipore). CD8<sup>+</sup> T cells (1 × 10<sup>6</sup>) were added on the chambers for 1 h and fixed with 4% PFA for 2 h. The samples were incubated with 1:100 anti-LFA-1 (H155-78, Biolegend) overnight at 4 °C. The samples were then incubated with 1:200 biotinylated goat anti-rat IgG (H + L; Vector Lab) for 1 h at room temperature, and samples were then incubated with 1:150 ExtrAvidin-horseradish peroxidase (E2886, Sigma-Aldrich) enzyme conjugate. The samples were presoaked in Tris buffer and DAB for 20 min, and hydrogen peroxide was added for 7 min. Labeled cells were washed and postfixed in 2% glutaraldehyde overnight before both silver and gold enhancement and postfixation in 1.0% OsO<sub>4</sub>. The labeled cells on the slides were dehydrated in a graded series of ethanol up to 100% and infiltrated with Spurr's epoxy resin overnight. Size 3 BEEM capsules were filled with epoxy resin and set up on top of the slides over the labeled cells for the 'Pop-off' technique. The resin was polymerized at 60 °C overnight. The capsules were 'popped off' the slides by dipping in liquid nitrogen to break the surface tension between the glass and the polymerized blocks containing the labeled cells. The blocks were trimmed to areas of cells and thin sectioned using a diamond knife at 70 nm onto formvar/carbon-coated

slot grids. The grids were examined and photographed using a Hitachi 7650 transmission electron microscope and a Gatan Erlangshen 11 megapixel digital camera system.

### RNA sequencing

RNA sequencing was performed as we previously described. Briefly, total RNA (1 ng) was preamplified with the SMARTer Ultra Low Input kit v4 per the manufacturer's recommendations (Clontech). We used a Qubit fluorometer (Life Technologies) and an Agilent Bioanalyzer 2100 to measure the quantity and quality of the subsequent cDNA. cDNA (150 pg) was used to generate Illumina-compatible sequencing libraries using a NexteraXT library preparation kit per the manufacturer's protocols (Illumina). We then hybridized the amplified libraries to the Illumina single-end flow cell and amplified them using the cBot (Illumina). Single-end reads (100 nucleotides) were generated. After filtering out genes with zero reads, genes between conditions were compared based on adjusted *P* values and log<sub>2</sub> fold change. DESeq2-1.22.1 within R-3.5.1 was used to perform data normalization and differential expression analysis with an adjusted *P* value threshold of 0.05 on each set of raw expression measures. The heat map and volcano plot were created using pheatmap (version 1.0.12) and pcaExplorer (versuib 2.8.0) with the DESeq2-normalized data and results. The Enrichr gene database was used to obtain categories of signaling pathways related to genes that were downregulated and upregulated in CART<sub>72</sub> compared to CART<sub>0</sub>. The listed categories were ranked by the likelihood that genes fall into the group as a function of *P* value. Principal-component analysis plots, volcano plots and heat map representations were produced using RStudio (version 1.3.1093, 2009–2020) or Graphpad Prism (v9).

### Intravitral microscopy

Intravitral microscopy was performed as we previously described<sup>48</sup>. Briefly, *in vivo* imaging was performed using an Olympus Fluoview FVMPE-RS Twin-Laser Gantry system with a ×25/1.05-NA water immersion objective (Olympus) and two lasers, the Spectra-Physics InsightX3 and MaiTai HP DeepSee Ti:Sapphire (University of Rochester Multiphoton Research Core Facility). Mice were anesthetized by intraperitoneally injecting pentobarbital sodium salt (65 mg kg<sup>-1</sup>). To restrain and avoid psychological stress and pain during imaging, mice were further maintained by isoflurane inhalation. For the lung image, non-recovery surgery on the lung and surrounding tissue was performed. First, three left anterior ribs of the mice were resected, and a small portion of the left lung was exposed; 20–25 mm Hg of suction was carefully applied to immobilize the part of lung within the thoracic suction window. The microscope objective was then placed over the thoracic suction window for live imaging. Depth of anesthesia was confirmed by monitoring of pain reflexes (pedal reflex), monitoring of respiratory rate before intubation, monitoring of respiratory pressure through a ventilator after intubation and monitoring of the heart rate and blood oxygenation via infrared pulse oximetry. An anesthesia record/surgery log was maintained throughout the procedure, and the paralytic was administered after the depth of anesthesia was confirmed. A cannula was put into place once the trachea was exposed and prepared. The cannula was attached to the ventilator once secured<sup>49</sup>. For dLNs, hair on the right hind leg and inguinal area of the mouse was removed by an electric trimmer. A small 2- to 3-mm incision with scissors was made at the right knee to expose the extensor tendon and then the right popliteal fossa. Subsequently, the right popliteal LN of the anesthetized mice was surgically exposed on the custom-designed platform. For ear (tumor) imaging, mice were anesthetized and laid flat on the custom-designed plate to expose the ear tumor under the coverslip onto the microscopy stage. To visualize blood vessels, PB- or Alexa Fluor 647-conjugated CD31 antibody was intravenously injected before the start of imaging. Images were obtained using Fluoview software (Olympus) at a resolution of 512 × 512 (16 bit). Each z stack was 2.5–3.5 µm apart at a frame rate of 1.5 s for a total of 40 frames.

Fluorescent signals were excited as follows: tdTomato: 975 nm; mRFP: 1,100 nm; Alexa Fluor 647: 1,200 nm; FITC/GFP: 975 nm (GFP) or 820 nm (FITC); BFP: 820 nm; and SHG: 850 nm. We also used the following filter cubes: red/Far-Red (575–630 nm/645–685 nm, DM650) and SHG/blue/green (420–460 nm/495–540 nm, DM485). We used Volocity (PerkinElmer), Imaris (Bitplane), Arivis Vision 4D (Arivis) and ImageJ software to process raw imaging data. For micro-PET/CT imaging of CART cell distribution,  $1 \times 10^7$  T cells were washed three times with PBS. After the final wash, cells were resuspended in 100  $\mu$ l of 0.1 M HEPES (pH 8) and incubated with SCN-Bz-Df for 30–60 min at 37 °C. Cells were then washed with PBS (pH 7.4) three times. After the final wash, cells were resuspended in 400  $\mu$ l of PBS (pH 6.5) and incubated with 20  $\mu$ l of  $^{89}\text{Zr}$  solution (in 1 M oxalic acid/1 M sodium carbonate) + 80  $\mu$ l of 0.5 M HEPES at room temperature for 1 h. After incubation, cells were washed three times with PBS (pH 7.4).

### Tissue clearing

ScaleCUBIC Reagent 1 (25 wt% urea, 25 wt% Quadrol and 15 wt% Triton X-100 in distilled water) and ScaleCUBIC Reagent 2 (50 wt% sucrose, 25 wt% urea and 10 wt% triethanolamine in distilled water) were prepared for tissue clearing<sup>50</sup>. To visualize blood vessels, PB-CD31 antibody was intravenously injected before lung extraction. After lung perfusion with cold PBS, whole-lung tissues were extracted and fixed with 4% PFA overnight. Whole-lung tissues were washed with PBS with shaking at room temperature and incubated in ScaleCUBIC Reagent 1 for 3 d at 37 °C with gentle shaking. After PBS washing, the tissues were stored in ScaleCUBIC Reagent 2 for 1 d at room temperature. For immunofluorescence staining, the tissues were stained with Alexa Fluor 594-hHER2, BV711-CD11c or BV711-MHC class II antibodies for 3 d at room temperature after tissue clearing with Reagent 1. After PBS washing, the tissues were incubated with ScaleCUBIC Reagent 2 for 1 d at room temperature. Images were acquired with an Olympus FluoView FVMPE-RS Twin-Laser Gantry system with a  $\times 10/1.05\text{-NA}$  water immersion objective (Olympus). Raw imaging data were processed and analyzed with Volocity (PerkinElmer), Arivis Vision 4D (Arivis) and ImageJ.

### CRISPR library construction

Five sgRNAs were designed against individual genes. The sgRNA oligonucleotides were synthesized (Collecta) and pooled in equal molarity. The pooled sgRNA oligonucleotides were then cloned into pMSCVURP-U6-sg-HTS6MC-UbiC-TagRFP-2A-Puro. We performed a deep-sequencing analysis and verified that >95% of the designed sgRNAs were cloned in the vector and >95% of individual sgRNA constructs were within fivefold of the mean. Transformation was performed using Invitrogen DH5a MAX efficiency cells following the manufacturer's protocol. Ten nanograms of library DNA was used in each reaction, and three reactions were performed in parallel. To calculate transformation efficiency, 10  $\mu$ l was taken from the pooled reactions and serially diluted to 1:50, 1:100 and 1:1,000 in SOC medium. Transformation efficiency was calculated by dividing the number of colonies counted on a given dilution plate by the number of micrograms used in the transformation and then multiplying by the dilution factor. We required a transformation efficiency 500 $\times$  the number of constructs in our library to proceed. Glycerol stocks were made from successfully transformed competent cells. In each 1-ml aliquot, there was at minimum 500 $\times$  library coverage based on cell number as determined by optical density at 600 nm of the overnight liquid culture. Cells were frozen in fresh culture medium with 25% glycerol by volume.

### Mouse experimental workflow for in vivo CRISPR screen

Retrovirus was produced using 293T Phoenix cells. To concentrate virus, Takara's RetroX Concentrator was used as per the manufacturer's protocol. To titrate virus, three different volumes of thawed

viral concentrate were used to infect 1 million T cells each. After 48 h, transduction efficiency was assessed using flow cytometry (RFP). The effective viral titer was calculated by multiplying the number of cells at the time of infection by the fraction of infected cells and dividing the product by the volume of virus used for infection. This process was repeated for each new batch of virus. CD8 $^+$  T cells were isolated from Cas9/OT-I donor mice and seeded on plates coated with anti-CD3/CD28 and cultured with the addition of IL-2 at 20 IU ml $^{-1}$  (day 0). On day 2, the cells were transduced with retroviral libraries and cultured with mouse IL-7 at 2.5 ng ml $^{-1}$ , mouse IL-15 at 25 ng ml $^{-1}$  and human IL-2 at 20 IU ml $^{-1}$  for 2 d. The transducer cells were selected with 3 mg ml $^{-1}$  for another 3 d. On day 7, transduction was assessed by flow cytometry, and  $3.5 \times 10^6$  cells were injected into recipient mice (B16-OVA tumor-bearing mice) intravenously. For all adoptive transfer experiments, CD8 $^+$  T cells from Cas9/OT-I mice were infected at a multiplicity of infection of 0.3 to achieve approximately 20% transduction efficiency using the techniques described above. On the day of transfer, an aliquot of infected cells totaling 500 $\times$  the library coverage was saved as an 'input' for comparison during later analysis of sgRNA enrichment. After 24 h, about  $7 \times 10^5$  Cas9/OT-I/sgRNA T cells were recovered from the lung/liver and spleen/LNs/blood ( $1.5 \times 10^5$  cells per group). T cells from five to six mice were pooled. We repeated this sample three times ( $n = 3$ ;  $n = 5$ –6 recipient mice per group).

### Analysis of pooled CRISPR screen

Analysis was performed as previously described<sup>51</sup>. Raw fastq files were cleaned and trimmed using cutadapt version 1.18 and aligned using bowtie version 1.2.2. Read counts for each sgRNA barcode were identified using featureCounts version 1.6.2. To identify hits from the screen, we used the MAGeCK software version 0.5.9 to quantify and test for guide enrichment<sup>52</sup>. Each assay was repeated three times. We then ran MAGeCK-MLE with three replicates ( $n = 3$ ;  $n = 5$ –6 mice per group) for each organ compartment (lung/liver (termed T<sub>Sequestered</sub>), spleen/LNs (termed T<sub>migratory</sub>) and baseline (non-infused, termed T<sub>0</sub>)). The P values and FDR of the  $\beta$ -scores shown in Fig. 2 were calculated using these replicated data sets for each compartment based on MAGeCK-MLE's maximum likelihood estimate<sup>53</sup>. The  $\beta$ -value for each gene represents the extent of selection for that gene in a particular condition (a positive  $\beta$ -value means that the gene is positively selected in that condition, and a negative  $\beta$ -value suggests negative selection). MAGeCK-MLE negative binomial distribution is used to also estimate a mean and z score for the estimated  $\beta$ -value. Data in Fig. 2b are a visualization of the z scores of the  $\beta$ -values for each of the target genes in the spleen/LNs and lung/liver tissues using MAGeCK-MLE. The genes are ranked by the z scores of their  $\beta$ -values within each condition and plotted. The x axis represents the rank of the genes based on their z scores, and the y axis represents the actual z scores. Genes with more negative z scores suggest strong negative selection in the reported tissue. The highlighted genes in the figure have an FDR of  $\leq 0.05$  (Wald test). The size of each highlighted point is scaled based on the  $-\log_{10}$  (FDR). Points with smaller FDR values are larger in size. MAGeCK-MLE is able to model complex experimental designs with multiple screening conditions. In our case, we used three screening conditions: lung/liver (T<sub>Sequestered</sub>), spleen/LNs (T<sub>migratory</sub>) and baseline (non-infused; T<sub>0</sub>). T<sub>0</sub> was used for MAGeCK-MLE's model building and for all sgRNA efficiency calculations. A positive  $\beta$ -score indicates positive selection, and a negative  $\beta$ -score indicates negative selection. The P values and FDR values of the  $\beta$ -scores were estimated using both a permutation test and a Wald test within the MAGeCK-MLE module. MAGeCK analysis for sgRNA, gene-level enrichment and normalized and raw count files can be found in the Source Data.

### Preparation of genomic DNA for next-generation sequencing

Amplification and barcoding of sgRNAs was performed following the manufacturer's specifications for constructing CRISPR pooled

lentiviral sgRNA libraries (Collecta). Briefly, an initial round of 25 cycles of PCR was performed using 100 ng of genomic DNA to amplify sgRNA sequences. Amplicons from the first PCR were used in a second PCR of nine cycles to add index, P5 and P7 sequences for Illumina sequencing. The final sequencing libraries were quantified using the Qubit double-stranded DNA assay (Thermo Fisher) and assessed for size using the Tapestation D1000 assay (Agilent). The pooled sequencing libraries were then size selected for the size range of 340–425 base pairs using the PippinHT (Sage Science). Libraries were sequenced on a NextSeq550 high-output flowcell (Illumina) to obtain single-end 50-nucleotide reads.

### Human samples

Peripheral blood mononuclear cells and plasma samples were collected from individuals with B cell lymphoma that received axicabtagene ciloleucel ( $2 \times 10^6$  cells per kg). Individuals provided consent for blood collection under the University of Rochester Medical Center Wilmot Cancer Center's lymphoma research program tissue collection protocol ULAB-03012 in accordance with the Institutional Review Board. Peripheral blood was obtained in sodium heparin tubes before treatment and after axicabtagene ciloleucel infusion from 40 individuals. Plasma was obtained by centrifugation of heparinized blood and stored at Wilmot Cancer Center of the University of Rochester. All stored aliquots of plasma were relabeled to a random, non-linked code before any analysis. These same individuals were undergoing CAR T cell therapy treatment. CAR T cells were prepared commercially and returned to the Wilmot Cancer Center for infusion. After infusion, some cells typically remained in the infusion tubing and storage bag. These cells are usually discarded but were recovered and used in the current studies. After completion of CAR T cell infusion, the infusion bag was washed with PBS to obtain residual cells. Plasma samples were also collected to measure IFN $\gamma$ , IL-6 and IL-1 $\beta$  levels using a xMAP human cytokine–chemokine magnetic bead panel kit (HCYTOMAG-60K, EMD Millipore) following the manufacturer's instructions. Briefly, participant plasma samples were thawed on ice 1 h before the experiment. The standards or plasma samples were pipetted (in duplicate) into 96-well Luminex plates. Next, 25  $\mu$ l of plasma samples was mixed and incubated with 25  $\mu$ l of specific color-coded antibody-linked magnetic beads for IFN $\gamma$ , IL-6 and IL-1 $\beta$  at room temperature on a shaker (800 r.p.m.) for 120 min. After adding biotinylated detection antibodies, the sample was incubated with streptavidin–PE. The plate was then washed twice using a Bio-Plex Pro magnetic wash station. Beads were resuspended in 125  $\mu$ l of Bio-Plex assay buffer before reading on a calibrated Bio-Plex 200 system (Bio-Rad). A five-parameter logistic curve was used, and data were analyzed with Bio-Plex Manager 6.0 software.

### Statistical analysis

All statistical tests were performed with GraphPad Prism (v9). Statistical analysis was performed using a Mantel–Cox test for survival curves, a two-way ANOVA, an ordinary one-way ANOVA with a Tukey's multiple-comparison post hoc test, an unpaired *t*-test and a Mann–Whitney test when appropriate. Differences were considered significant when *P* values were  $<0.05$ . No statistical methods were used to predetermine sample sizes, but our sample sizes are similar to those reported in previous publications<sup>48</sup>. Data distribution was assumed to be normal, but this was not formally tested. In all *in vivo* experiments, C57BL/6 mice and transgenic mice (male or female) aged 7–10 weeks were age and sex matched and randomly assigned to each group. For the *in vitro* assays, samples and cell conditions were randomly distributed across treatment groups. For *in vivo* experiments, there was no blinding in collection and analysis of the experimental data due to requirements for cage labeling and staffing needs. For *in vitro* experiments, all the treatments were performed in a parallel manner without the risk of bias

in interpretation. All data were acquired and analyzed by software with object standard. Therefore, blinding was not relevant to the study. No data were excluded from the study.

### Reporting summary

Further information on research design is available in the Nature Portfolio Reporting Summary linked to this article.

### Data availability

The Protein Data Bank accession code is [SE6U](#). Signaling pathway analysis was performed with Enrichr using the NCI-Nature 2016 database for pathway enrichment analysis (<http://amp.pharm.mssm.edu/Enrichr>). Sequencing datasets have been deposited in the Gene Expression Omnibus database under accession codes [GSE227429](#) (CRISPR screen), [GSE227509](#) (CD8 $^+$  T cell bulk RNA sequencing) and [GSE227430](#) (CAR T cell bulk RNA sequencing). All other data are included in the article and Supplementary Information files. Source data are provided with this paper.

### References

45. Potrzebowska, K., Lehtonen, J., Samuelsson, M. & Svensson, L. Flow cytometry assay for recycling of LFA-1 in T-lymphocytes. *Bio Protoc.* **8**, e3104 (2018).
46. Morin, N. A. et al. Nonmuscle myosin heavy chain IIA mediates integrin LFA-1 de-adhesion during T lymphocyte migration. *J. Exp. Med.* **205**, 195–205 (2008).
47. Bern, M., Kil, Y. J. & Becker, C. Byonic: advanced peptide and protein identification software. *Curr. Protoc. Bioinformatics* **40**, 13.20.11–13.20.14 (2012).
48. Lim, K. et al. *In situ* neutrophil efferocytosis shapes T cell immunity to influenza infection. *Nat. Immunol.* **21**, 1046–1057 (2020).
49. Looney, M. R. et al. Stabilized imaging of immune surveillance in the mouse lung. *Nat. Methods* **8**, 91–96 (2011).
50. Susaki, E. A. et al. Advanced CUBIC protocols for whole-brain and whole-body clearing and imaging. *Nat. Protoc.* **10**, 1709–1727 (2015).
51. Shifrut, E. et al. Genome-wide CRISPR screens in primary human T cells reveal key regulators of immune function. *Cell* **175**, 1958–1971 (2018).
52. Li, W. et al. MAGeCK enables robust identification of essential genes from genome-scale CRISPR/Cas9 knockout screens. *Genome Biol.* **15**, 554 (2014).
53. Li, W. et al. Quality control, modeling, and visualization of CRISPR screens with MAGeCK-VISPR. *Genome Biol.* **16**, 281 (2015).

### Acknowledgements

We thank the High Content Image Core (University of Rochester) for help with fluorescence imaging and use of the Dragonfly spinning-disc confocal. We thank Y. Gao and P. Rock for their technical assistance on the manuscript. We especially thank M. Jin (Weill Cornell) for the anti-HER2 CAR DNA construct and for his help with micro-PET/CT imaging, L. Gan (Augusta University) for help with  $\beta$ II-spectrin transgenic mouse generation, R. Burack and J. Moore for human sample collections and data review, J. Ashton, D. Ghoneim and J. Malik for help with CRISPR transcriptomic analyses and depositing RNA-sequencing data and all members of the Kim Laboratory for their comments during the course of these studies and input during preparation of the manuscript. We obtained hHER2 transgenic mice from Genentech. This study was funded by National Institutes of Health grant AI102851 (M.K. and P.W.O.), National Institutes of Health grant AI147362 (M.K. and R.E.W.), National Institutes of Health grant T32AI007285 (A.M.A. and C.J.S.), National Science and Technology Council in Taiwan MOST 111-2314-B-182A-069 and MOST 111-2321-B-182-002 (T.-C.F.) and K-GRC GO! KRICT project BSF23-113 (K.-D.K.).

## Author contributions

Conceptualization: Y.H., H.-R.K., B.L.W. and M.K. methodology: Y.H., H.-R.K., B.L.W., W.S.S., M.K., J.R.L., A.M.A., C.J.S., K.L., R.K.M., K.-D.K., T.C., E.B.L., N.S.R., K.V., T.-C.F., A.L.-T.Y., P.W.O., R.E.W., C.-D.J., P.M.R. and S.A.G. investigation: Y.H., H.-R.K., B.L.W., W.S.S., J.R.L., A.M.A., C.J.S., K.L., K.-D.K., T.C., E.B.L., N.S.R., K.V. and T.-C.F. funding acquisition: A.M.A., P.W.O., M.K., R.E.W. and K.-D.K. supervision: M.K. writing, original draft: Y.H., H.-R.K., B.L.W. and M.K.

## Competing interests

The authors declare no competing interests.

## Additional information

**Extended data** is available for this paper at <https://doi.org/10.1038/s41590-023-01498-x>.

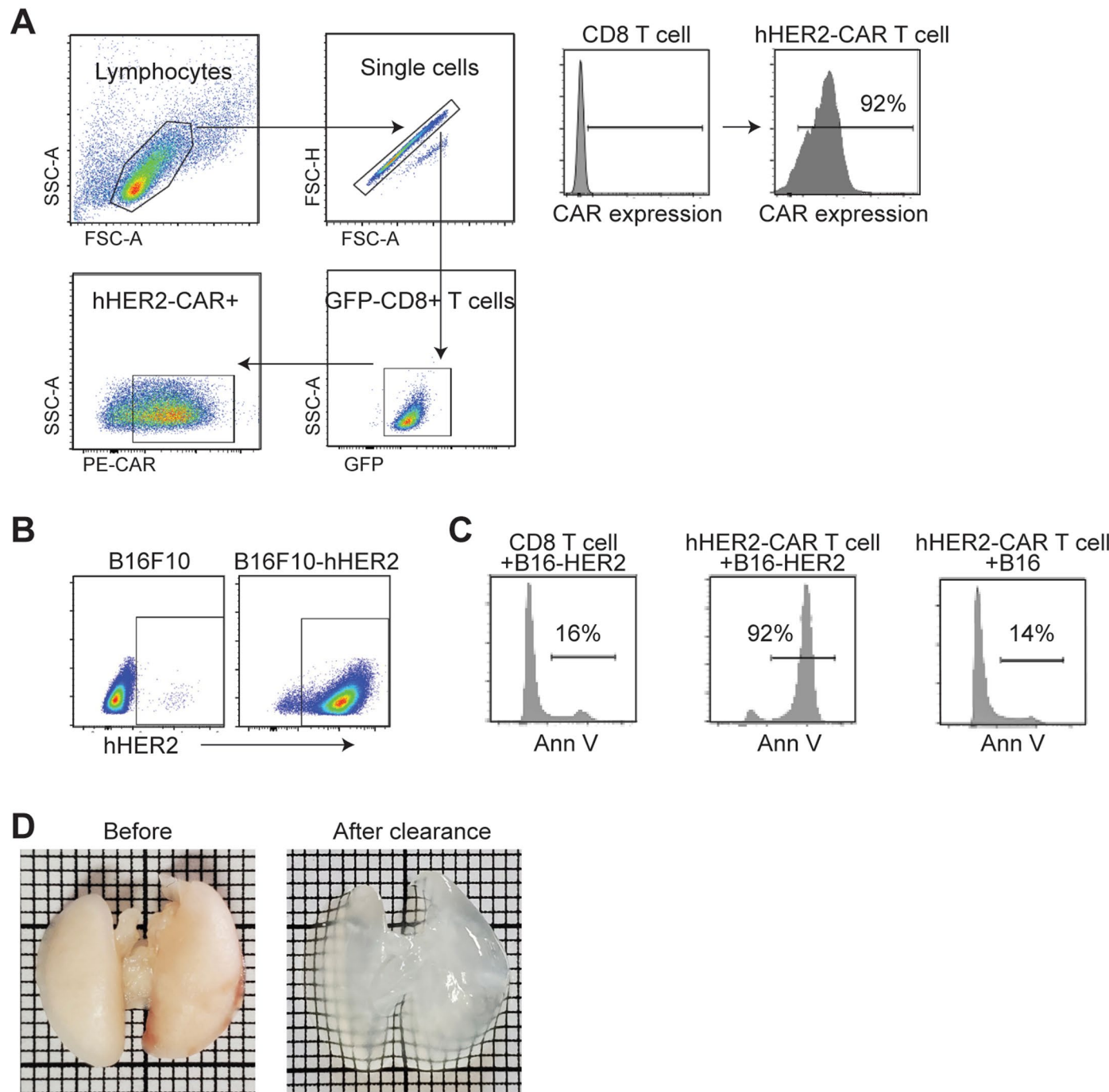
## Supplementary information

The online version contains supplementary material available at <https://doi.org/10.1038/s41590-023-01498-x>.

**Correspondence and requests for materials** should be addressed to Minsoo Kim.

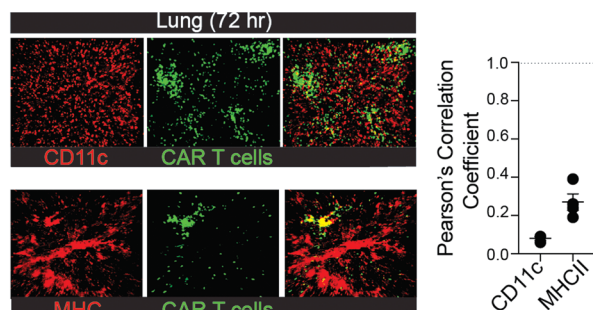
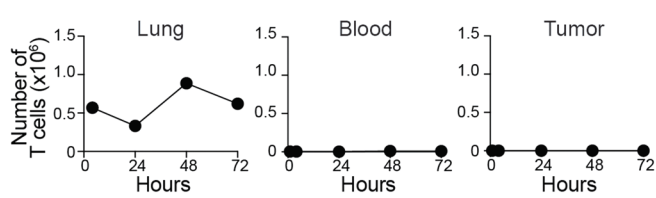
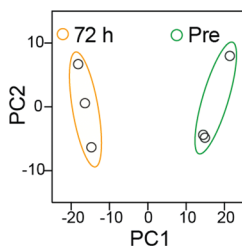
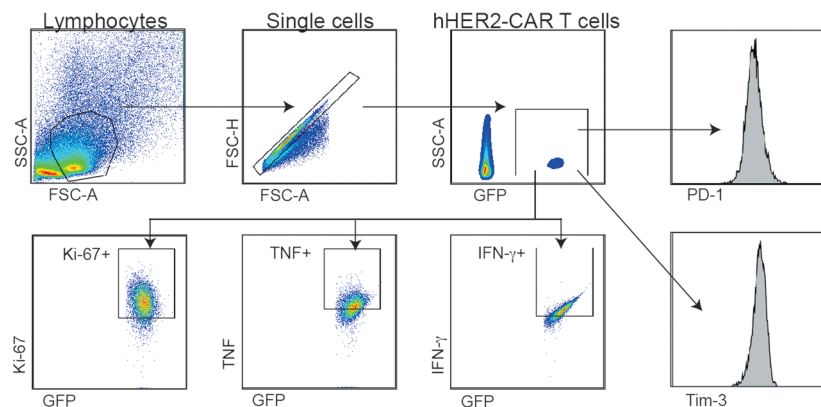
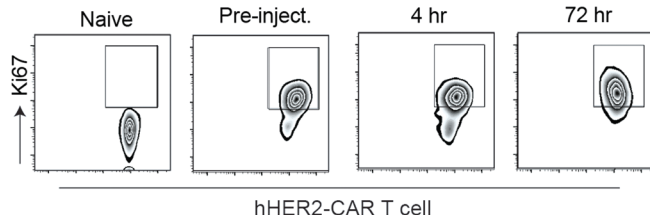
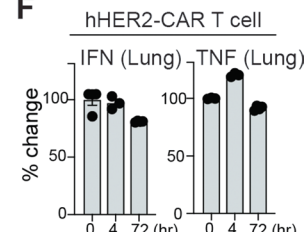
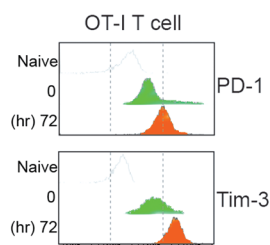
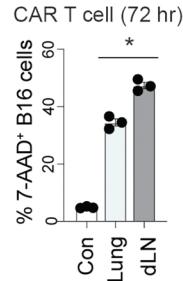
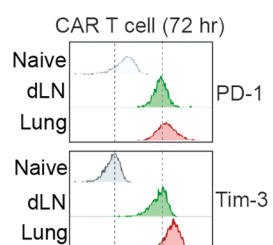
**Peer review information** *Nature Immunology* thanks Michael Sixt, Joy Burchell, and the other, anonymous, reviewer(s) for their contribution to the peer review of this work. Primary Handling Editor: N. Bernard, in collaboration with the *Nature Immunology* team.

**Reprints and permissions information** is available at [www.nature.com/reprints](http://www.nature.com/reprints).



**Extended Data Fig. 1 | hHER2 CAR-T cell assays and in vivo distribution.** **a.** Gating strategy for detection of hHER2-CAR-T cells. A median of > 90% of mouse CD8 T cells transduced with the hHER2-CAR retrovirus were positive for the transgene as judged by flow cytometry analysis. **b.** B16F10 cells were transfected with mammalian human HER2 construct with lipofectamine. Cells were grown in

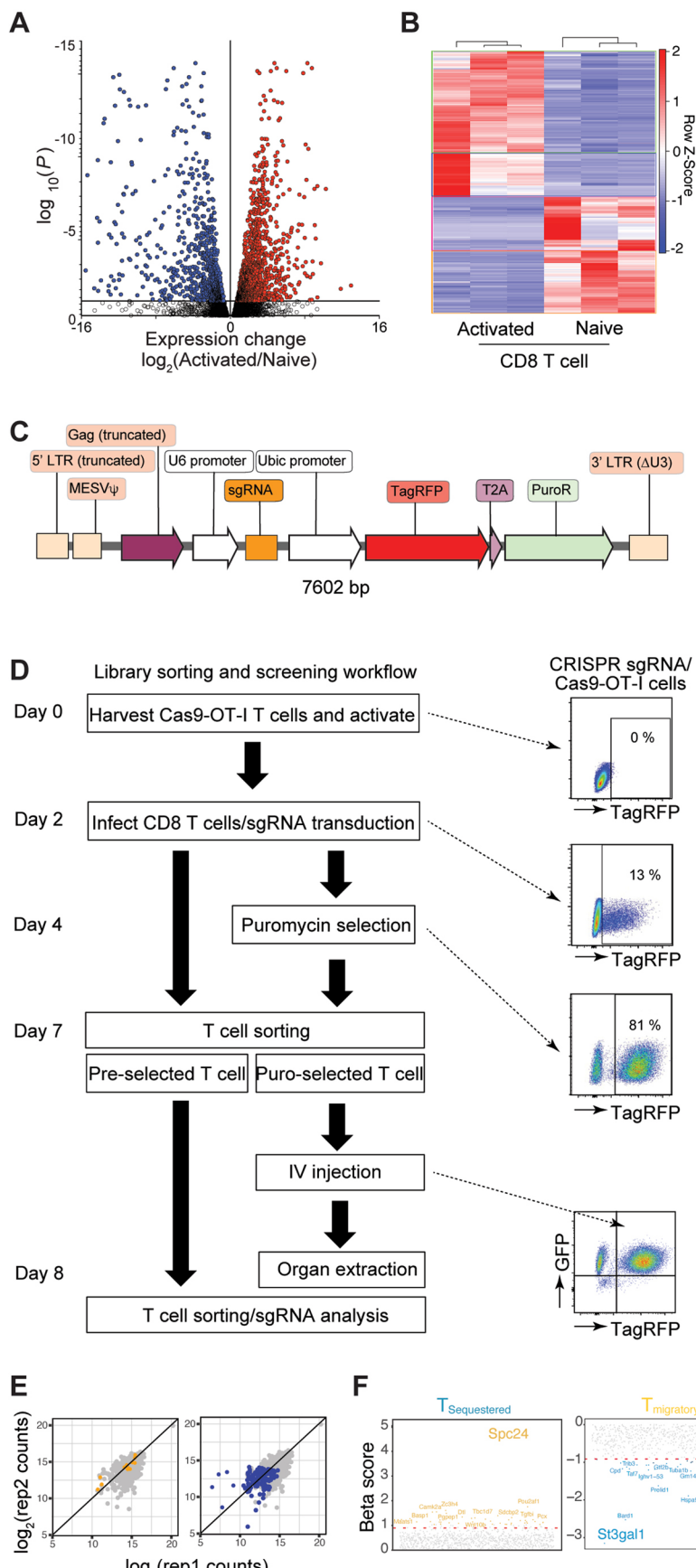
the presence of G418 and sorted twice to generate single cell clones. **c.** CAR-T-mediated B16-HER2 cell killing assay. Apoptotic cells were stained for Annexin V and analyzed by flow cytometry. **d.** Whole mouse lung before and after CUBIC clearing.

**A****B****C****D****E****F****G****H****I**

Extended Data Fig. 2 | See next page for caption.

**Extended Data Fig. 2 | hHER2 CAR-T cell distribution.** A. Deep 3D imaging (1 mm thick) of CAR-T cell accumulation in the cleared mouse lung after 72 hr after i.v. injection (red; CD11c or MHCII, green; CAR-T cell). Graph shows colocalization of red signal versus GFP (CAR-T cells). Pearson coefficient was generated as Green (CAR-T cell)/Red (anti-CD11c or anti-MHCII). Data are presented as mean  $\pm$  SEM; n = 3 mice/group. B. Flow cytometric analysis of OT-I T cells in the lung, blood, and tumor after i.v. injection (4, 24, 48, and 72 hr; mean  $\pm$  SEM, n = 3 mice per group). C. PCA of differentially expressed genes in CAR-T cells ( $T_{72}$  vs.  $T_0$ ). D. Gating strategy for detection of hHER2-CAR-T cells from organs (**lungs**). E. Expression of Ki67+ in CAR-T cells isolated from the lung after i.v. injection. F. Relative expression of IFN- $\gamma$  and TNF in CAR-T cells isolated from

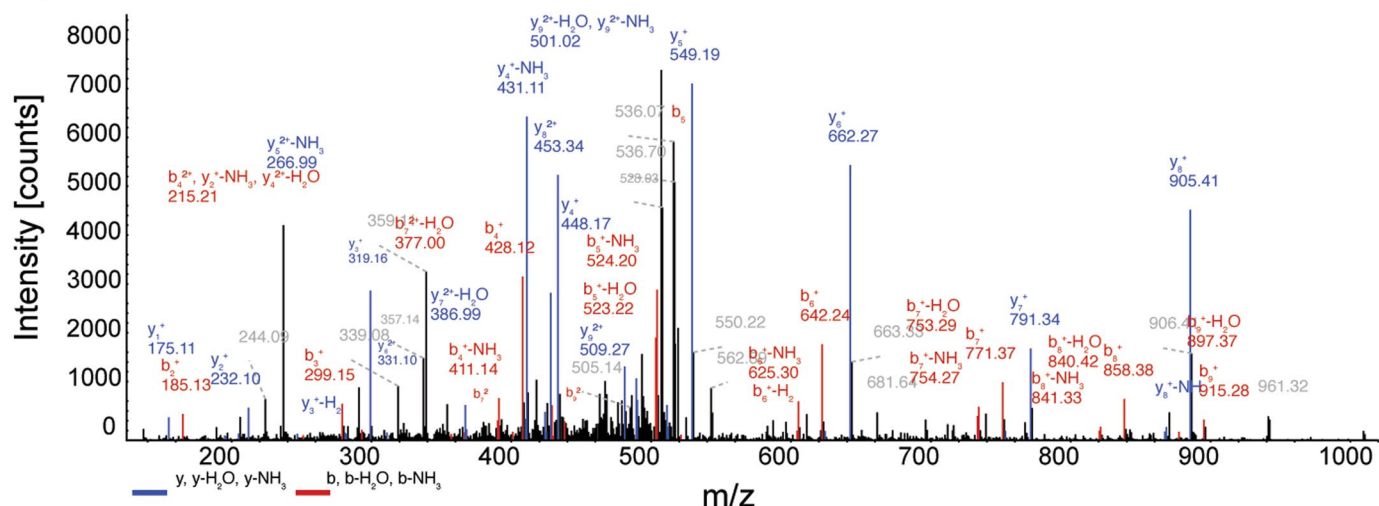
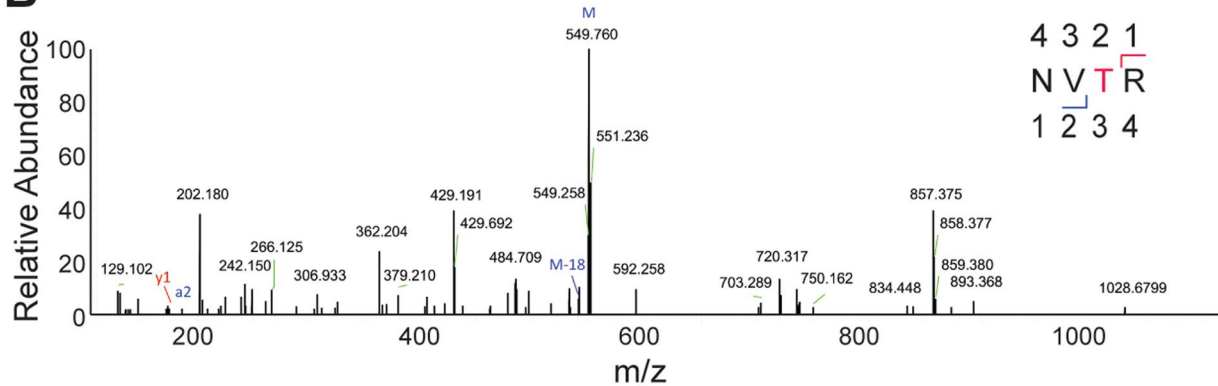
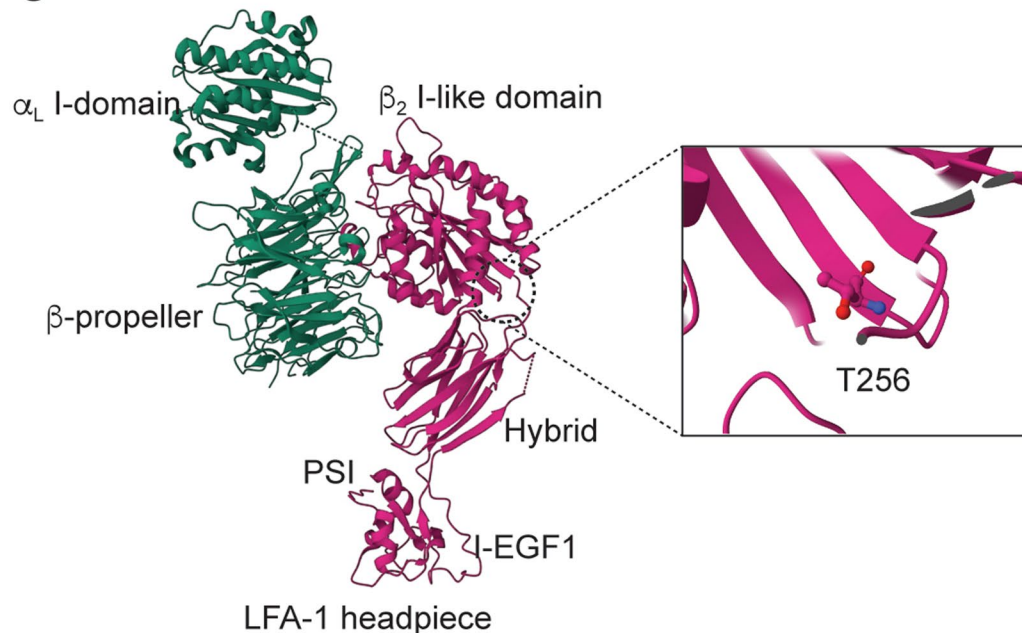
lung at indicated times after i.v. injection. Data are presented as mean  $\pm$  SEM; n = 3 mice/group. G. Representative flow cytometry results show cell surface PD-1 and Tim-3 expression levels in OT-I naïve T cells, freshly activated *in vitro* (0 hr), or isolated from the lung after 72 hr post-injection. H. hHER2-CAR-T cells isolated from the lung or dLN after 72 hr i.v. injection were cocultured with B16-hHER2 for 24 hr. Dead B16 cells were stained with 7-AAD. The data reflect 3 independent experiments (the mean  $\pm$  SEM, n = 3). The data were analyzed by two-tailed Student's t test (\*P = 0.002). I. Representative flow cytometry results showing cell surface PD-1 and Tim-3 expression levels in naïve and CAR-T cells isolated from the lung at the indicated times post-injection.



Extended Data Fig. 3 | See next page for caption.

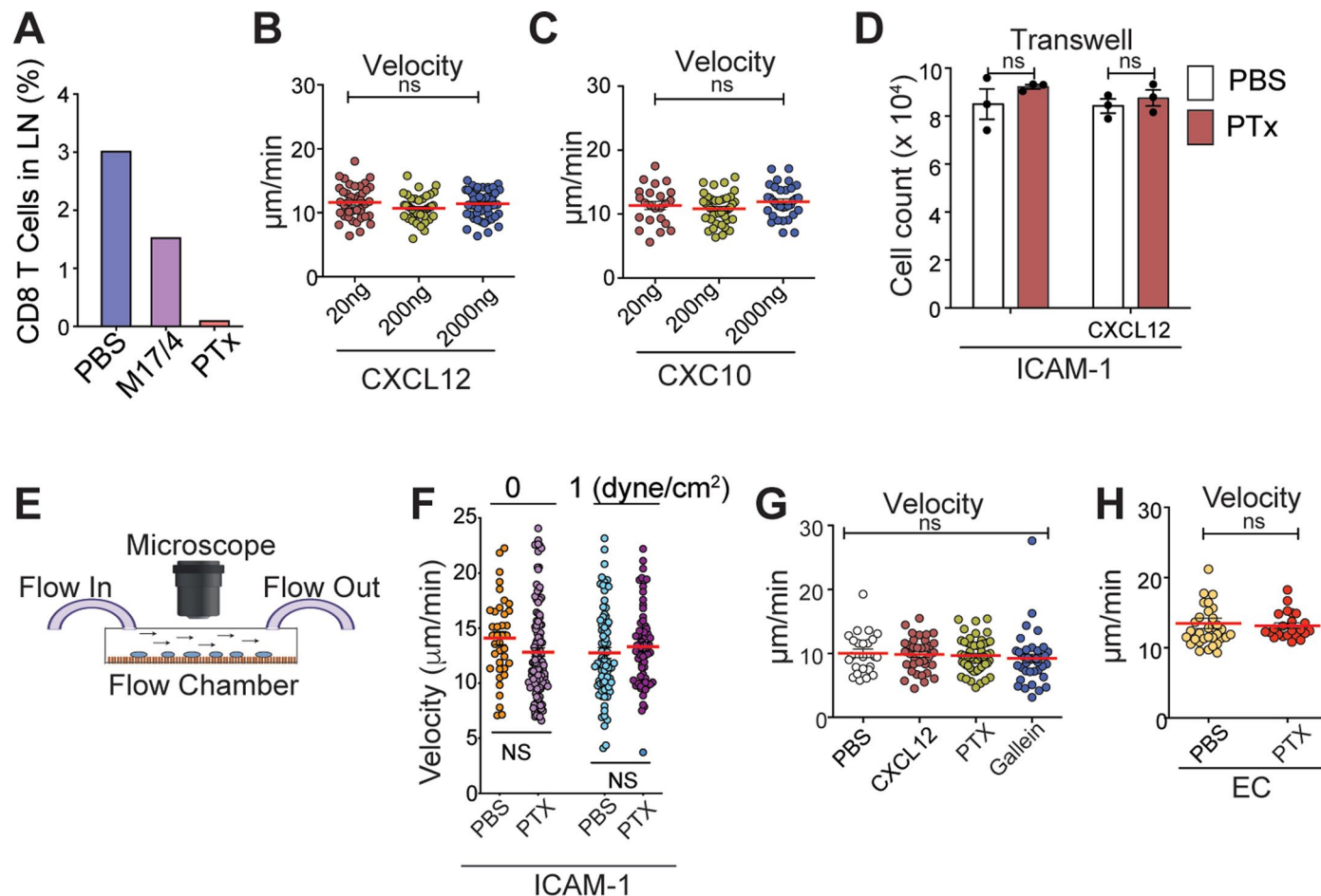
**Extended Data Fig. 3 | In vivo T cell CRISPR screen.** **a.** Volcano plot shows comparison of differentially expressed genes in naïve vs. *in vitro* activated CD8 T cells. Red denotes genes increased and blue denotes genes decreased in T cells. P values were adjusted using the Benjamini–Hochberg method. **b.** Heatmap of RNA-seqencing data from naïve vs. *in vitro* activated CD8 T cell samples ( $n = 3$ ). Heatmap represents top 1,316 genes chosen from highest 0.25% p-value summary. **c.** Retroviral construct used for sgRNA delivery. **d.** A schematic of the experimental design showing timeline of T cell stimulation, transduction,

enrichment, and flow analysis. T cells were purified by FACS sorting at day 7 and i.v injected into recipient tumor bearing mice. **e.** Scatter plot of the enrichment of candidates ( $n = 5$  sgRNAs per gene) showing that sgRNAs targeting essential genes (*left*) were significantly reduced in the samples after two representative *in vivo* screens, but not the non-targeting guides (*right*). **f.** Genes with positive beta score ( $T_{\text{migratory}}$ ) and negative beta score ( $T_{\text{sequestered}}$ ) ( $>2$  standard deviations from the mean (red)) are highlighted in yellow and blue, respectively.

**A****B****C**

**Extended Data Fig. 4 | Identification of CD18.** **a.** The spectrum of one of the CD18 peptides obtained by nanospray-ion trap tandem mass spectrometry. **b.** The deconvoluted MS/MS spectrum of tryptic peptide NVTR with 3 HexNAc. M: the parent ion of NVTR-HexNAc(3) at  $m/z$  549.760 Da. M-18: loss one  $H_2O$  in

NVTR-HexNAc(3). a2: the observed  $m/z$  186.1218 Da matched to the a2 ion. y1: the observed  $m/z$  175.1261 Da matched to the y1 ion. **c.** The crystal structure of LFA-1 headpiece (SE6U.pdb). The region encircled by dots from the left view is enlarged (right), representing the O-glycosylation on Thr256 in  $\beta$ I-domain.



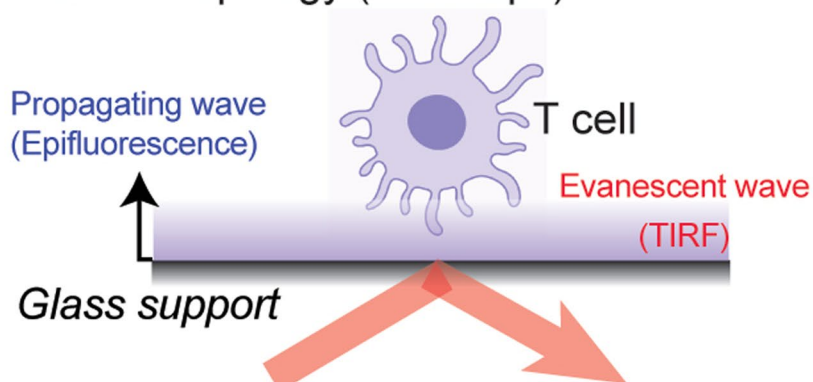
**Extended Data Fig. 5 | Activated T cell migration in vitro.** **a.** Recruitment of CAR-T cells into dLN was blocked by LFA-1-blocking Ab and PTx treatments. Percentages of total transferred CD8 + T cells are shown. **b & c.** Activated CD8<sup>+</sup> T cell migration on ICAM-1-coated plates ± CXCL12 (B) or CXCL10 (C) with varying concentrations as indicated. Data were collected from 3 independent experiments (n = 3, 11–20 individual cells per mouse). Data represent mean ± SEM. Statistical analyses were performed using one-way ANOVA with Bonferroni post-test. **d.** Representative Transwell assay of *in vitro* activated CD8<sup>+</sup> T cell migration in response CXCL12 (2  $\mu\text{g}/\text{ml}$ ). Data were collected from 3 independent experiments (1  $\times 10^6$  cells/well). Data represent mean ± SEM. Statistical analyses were performed using two-sided, unpaired Student's t test. **e.** Schematic depicting the flow chamber assay. **f & g.** Activated CD8<sup>+</sup> T cell migration on ICAM-1 coated plates with flow. Cells were treated with PTx (6 h)

(F) and/or gallein (30 min) (G) ± CXCL12 (G) where indicated. Cells were allowed to settle for 10 minutes prior to 1 dyne/cm<sup>2</sup> of fresh media being run across the surface of the plate. Data were collected from 3 independent experiments (n = 3, 25–45 individual cells per mouse). Data represent mean ± SEM. Statistical analyses were performed using one-way ANOVA with Bonferroni post-test.

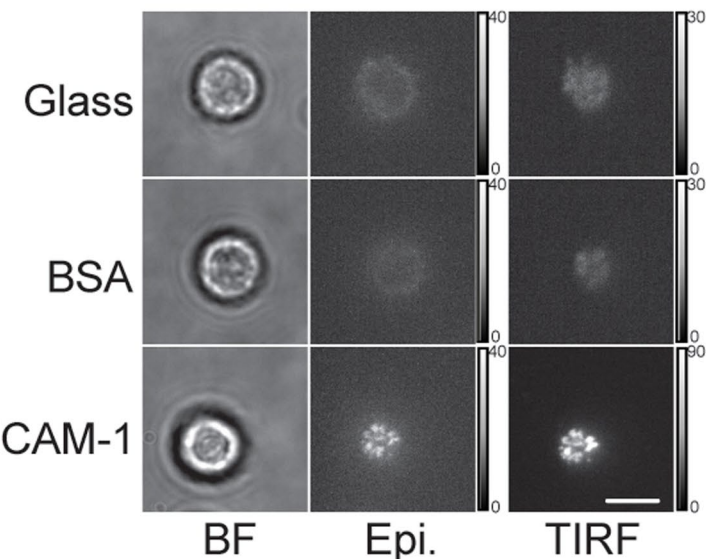
**h.** Activated CD8<sup>+</sup> T cell migration on bEND.3 coated plates. bEND.3 cells were allowed to grow to a monolayer for at least 12 h prior to imaging. CD8<sup>+</sup> were treated with PTx (6 h) where indicated. T cells were allowed to settle for 10 minutes prior to 1 dyne/cm<sup>2</sup> of fresh media being run across the surface of the plate. Data were collected from 3 independent experiments (n = 3, 20–39 individual cells per mouse). Data represent mean ± SEM. Statistical analyses were performed using two-sided, unpaired Student's t test.

**A**

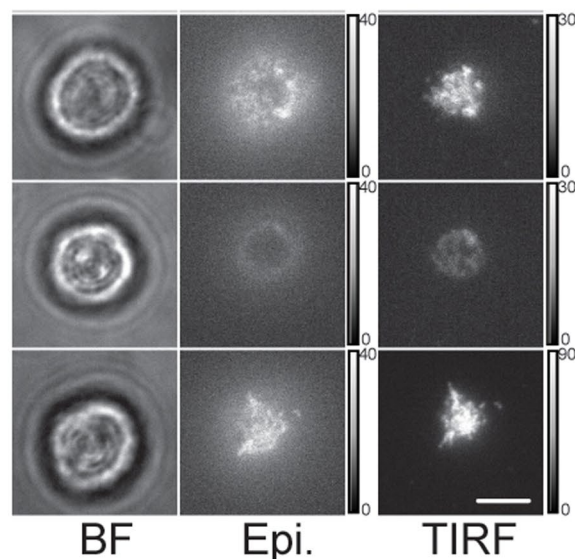
## LFA-1 topology (TIRF/Epi.)

**B**

## CD8 T cell (naive)

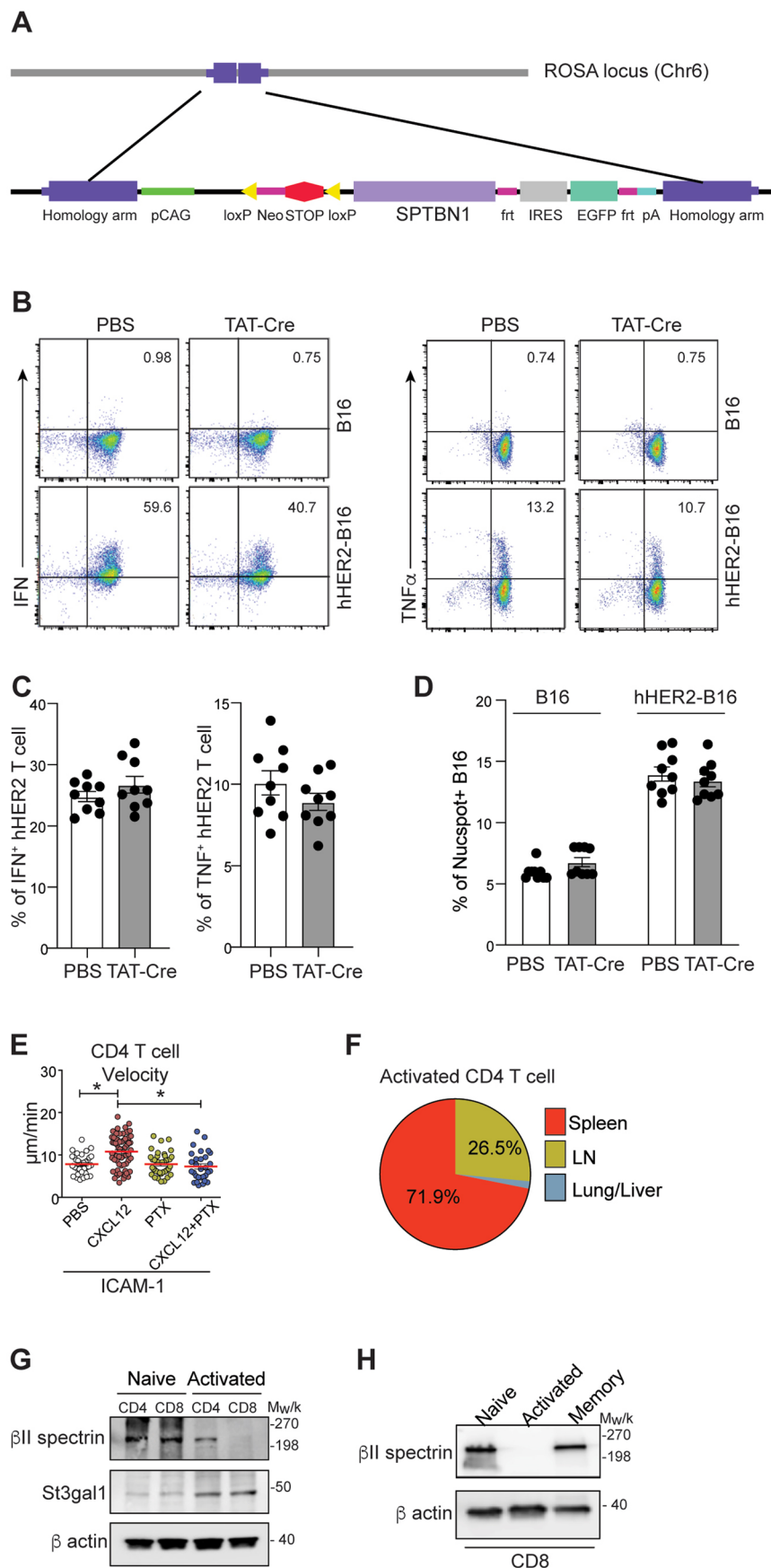


## CD8 T cell (activated)



**Extended Data Fig. 6 | TIRFM measurements of LFA-1 distribution. a.** Schematic of TIRFM measurements. Molecules near the surface fluoresce more brightly than molecules between microvilli and those farther from the substrate. **b.** Human CD8 T cells labeled for LFA-1 spreading on glass, BSA, or ICAM-1 coated

substrate. Contrast and brightness have been adjusted for visibility, but the original gray values are indicated in the scale bars to the right of each image. All images in the same row are at the same magnification. Scale bars, 5  $\mu$ m. Representative images from > five independent experiments are shown.



Extended Data Fig. 7 | See next page for caption.

**Extended Data Fig. 7 |  $\beta$ II-spectrin expression in T cells.** **a.** Generation of GFP-ROSA $^{\beta$ II-spectrin} mouse model (Rosa26<sup>tm1</sup>(CAG-LSL-Sptbn1-IRES-GFP)). Mouse Sptbn1 cDNA was inserted into the CAG-STOP-GFP-Rosa targeting vector, CTV, between a floxed Stop cassette and the internal ribosome entry site (IRES) followed by the enhanced Green Fluorescent Protein gene (eGFP). Transcription is under control of the CAG promoter. The targeting vector contained Rosa26 homology arms (1 kb 5' and 3.8 kb 3'), so that the entire loxP-stop-loxP-Tmc2-IRES-GFP transcriptional cassette was inserted into the first intron of Rosa26 gene on chromosome 6. **b & c.** Flow cytometry analysis of IFN $\gamma$  and TNF expression in hHER2-CAR transfected T cells from GFP-ROSA $^{\beta$ II-spectrin} mouse ( $T_{\beta$ II-spectrin}) after treated with PBS or Tat-Cre Recombinase. Cells were co-cultured with B16-HER2 cells. Data represent mean  $\pm$  SEM. n = 9. **d.** CAR-mediated B16-HER2 cell killing assay with  $T_{\beta$ II-spectrin> cells after treated with PBS or Tat-Cre Recombinase.

Cell death was stained for NucSpot. Data represent mean  $\pm$  SEM. n = 9. **e.** Activated CD4 $^{+}$  T cell (OT-II) migration on ICAM-1 coated plates  $\pm$  CXCL12. Cells were treated with PTx (6 hr) where indicated. Data were collected from 2 independent experiments (n = 2, 17–34 individual cells per mouse). Data represent mean  $\pm$  SEM Statistical analyses were performed using one-way ANOVA with Bonferroni post-test. \*P = 0.007. **f.** The pie charts depict the proportion of CD4 T cells distributed in the tumour, blood, LN/spleen, or lung/liver 72 h post-injection. **g.** Expression levels of  $\beta$ II-spectrin and St3gal1 in human CD4 and CD8 T cells (before and after activation). Loading control:  $\beta$ -actin. Representative western blot images from three independent experiments are shown. **h.** Expression levels of  $\beta$ II-spectrin in human CD8 memory T cells (CD8 $^{+}$ CD45RO $^{+}$ CD45RA $^{-}$ CD56 $^{-}$ CD57 $^{+}$ ). Loading control:  $\beta$ -actin. Representative western blot images from three independent experiments are shown.

## Reporting Summary

Nature Portfolio wishes to improve the reproducibility of the work that we publish. This form provides structure for consistency and transparency in reporting. For further information on Nature Portfolio policies, see our [Editorial Policies](#) and the [Editorial Policy Checklist](#).

### Statistics

For all statistical analyses, confirm that the following items are present in the figure legend, table legend, main text, or Methods section.

n/a Confirmed

- The exact sample size ( $n$ ) for each experimental group/condition, given as a discrete number and unit of measurement
- A statement on whether measurements were taken from distinct samples or whether the same sample was measured repeatedly
- The statistical test(s) used AND whether they are one- or two-sided  
*Only common tests should be described solely by name; describe more complex techniques in the Methods section.*
- A description of all covariates tested
- A description of any assumptions or corrections, such as tests of normality and adjustment for multiple comparisons
- A full description of the statistical parameters including central tendency (e.g. means) or other basic estimates (e.g. regression coefficient) AND variation (e.g. standard deviation) or associated estimates of uncertainty (e.g. confidence intervals)
- For null hypothesis testing, the test statistic (e.g.  $F$ ,  $t$ ,  $r$ ) with confidence intervals, effect sizes, degrees of freedom and  $P$  value noted  
*Give P values as exact values whenever suitable.*
- For Bayesian analysis, information on the choice of priors and Markov chain Monte Carlo settings
- For hierarchical and complex designs, identification of the appropriate level for tests and full reporting of outcomes
- Estimates of effect sizes (e.g. Cohen's  $d$ , Pearson's  $r$ ), indicating how they were calculated

*Our web collection on [statistics for biologists](#) contains articles on many of the points above.*

### Software and code

Policy information about [availability of computer code](#)

#### Data collection

Intravital multiphoton microscopy (IV-MPM) imaging was performed using an Olympus Fluoview FVMPE-RS Twin-Laser Gantry system and two lasers, Spectra-Physics InsightX3 and MaiTai HP DeepSee Ti:Sapphire. Microscopy was conducted using a TE2000-U microscope (Nikon) and a 10x magnification objective. Cells were analyzed using an LSRII 18 color flow cytometer (BD Bioscience). Cas9/OT1 T cells and CD8+ T cells were cell sorted using a FACS Aria (BD Bioscience). qPCR was performed with CFX96 Real-Time PCR machine (Bio-Rad Laboratories)

#### Data analysis

Post-image processing and data analysis were performed using Volocity (PerkinElmer), Imaris (Bitplane), Arivis Vision 4D (Arivis), Matlab (Mathworks) and ImageJ (1.53t). Crispr screen data was analyzed using Cutadapt (v1.18), Bowtie (v1.2.2), featureCounts (v1.6.2), MAGeCK (v0.5.9), which is publicly available. RNA sequencing data was analyzed using DESeq2 (v1.22.1), which is publicly available. The heat map, volcano plot were created using pheatmap (v1.0.12) and pcaExplorer(v2.8.0). Gene clustering, heat map, PCA plot, and volcano plot representations were produced using RStudio (v1.3.1093, 2009-2020) and Graphpad Prism (v9). Flow cytometry data was analyzed using FlowJo software (v10). Statistical tests was done using Graphpad Prism (v9).

For manuscripts utilizing custom algorithms or software that are central to the research but not yet described in published literature, software must be made available to editors and reviewers. We strongly encourage code deposition in a community repository (e.g. GitHub). See the Nature Portfolio [guidelines for submitting code & software](#) for further information.

## Data

Policy information about [availability of data](#)

All manuscripts must include a [data availability statement](#). This statement should provide the following information, where applicable:

- Accession codes, unique identifiers, or web links for publicly available datasets
- A description of any restrictions on data availability
- For clinical datasets or third party data, please ensure that the statement adheres to our [policy](#)

All data analyzed during the present study are included in this article and its supporting information files. Source data are provided in this paper. PDB accession code is 5E6U. Signaling pathway analysis was performed with Enrichr using NCI-Nature 2016 database for pathway enrichment analysis (<http://amp.pharm.mssm.edu/Enrichr>). Sequencing datasets have been deposited in the Gene Expression Omnibus database under accession codes GSE227429 (CRISPR screen), GSE227509 (CD8 T cell bulk RNA-seq) and GSE227430 (CAR-T cell bulk RNA-seq) and are publicly available.

## Human research participants

Policy information about [studies involving human research participants and Sex and Gender in Research](#).

### Reporting on sex and gender

This study is aimed at understanding fundamental behavior of normal and activated T cells. As such, it does not seek to answer questions related to differences among different subject populations or groups having different characteristics or subjected to different procedures. Therefore, the number of subjects who donate blood is not directly related to the objectives of the research except to provide adequate diversity in the subject population. Donors in our study can be male or female and between the ages of 18 and 70. Our ability to diversify the subject population is limited by the availability of individuals willing to donate. Within this constraint, we make every attempt to obtain equal representation according to sex. However, sex and gender is not a factor in our data analyses as it is well-known that sex does not significantly affect cytotoxic functions of CD8 T cells. Sex and/or gender of participants was determined based on self-report.

### Population characteristics

All the demographics and clinical characteristics of the participants can be found in Supplementary Table 7.

### Recruitment

Two sources of human cells were used in our studies: (CAR)-T cells discarded after immunotherapy treatment of patients, and T cells isolated from human healthy and patient donors.

#### <Discarded cells and plasma samples>

In our current IRB approved studies, peripheral blood mononuclear cells (PBMCs) and plasma samples are being collected from patients with diffuse large B-cell lymphoma that received commercial axicabtagene ciloleucel (2 x 10<sup>8</sup> cells/kg).

#### Eligibility Criteria:

1. Diagnosis of diffuse large B-cell lymphoma and related aggressive B-cell lymphomas such as high grade B-cell lymphoma and transformed indolent lymphoma
2. Age >18 years
3. Plan to receive commercial axicabtagene ciloleucel for relapsed or refractory aggressive B-cell lymphomas
4. Ability to provide informed consent.

Patients consent for blood collection under the University of Rochester Medical Center Wilmot Cancer Center's lymphoma research program tissue collection protocol ULAB-03012 in accordance with the Institutional Review Board.

#### <T cells from patient and healthy volunteers>

T cells were obtained from whole blood samples drawn freshly from patients and healthy volunteers by venipuncture performed by a qualified technician.

#### Subject Population:

Sex and age. Donors can be male or female and between the ages of 18 and 70. Our ability to diversify the subject population is limited by the availability of individuals willing to donate. Within this constraint, we made every attempt to obtain equal representation according to sex. Within the specified range, age is not a factor in selecting volunteers.

Race and Ethnic origin. We have no restrictions on participation based on race or ethnic origin. We attempted to make the subject population as diverse as possible within the constraints of voluntary participation.

Inclusion and exclusion criteria: Our criteria for normal donors are that they be in good health and willing to donate.

### Ethics oversight

Patients consent for blood collection under the University of Rochester Medical Center Wilmot Cancer Center's lymphoma research program tissue collection protocol ULAB-03012 in accordance with the Institutional Review Board. The Human Research Studies Review Board of the University of Rochester approved this study, and informed consent was obtained in accordance with the Declaration of Helsinki.

Note that full information on the approval of the study protocol must also be provided in the manuscript.

## Field-specific reporting

Please select the one below that is the best fit for your research. If you are not sure, read the appropriate sections before making your selection.

Life sciences

Behavioural & social sciences

Ecological, evolutionary & environmental sciences

# Life sciences study design

All studies must disclose on these points even when the disclosure is negative.

Sample size	Group size for in vivo validation experiments were selected empirically based on previous results of the intra-group variation of T cell responses and tumor growth. Sample sizes were selected to be appropriate based on the scale and consistency of measurable differences between groups. Usually 4 - 10 mice per group are sufficient to detect the significantly biological differences with good reproducibility. For in vitro experiments, group size were selected on the basis of previous publication and prior knowledge of variation. All the in vitro experiments were replicated at least 3 individual and independent experiments. For Fig. 3B, sample size was determined based on previous experiments from other groups (i.e. Giovannone et al. <i>Frontiers in Immunology</i> 2018).
Data exclusions	Data were not excluded.
Replication	We confirmed that all results were reliably reproduced for each experiment and the number of experimental replicates are indicated in the figure legends. Attempts at replication were successful once the conditions of the experiment were carefully optimized with pilot experiments.
Randomization	In all in vivo experiments, C57BL/6 mice and transgenic mice with male or female mice aged 7-10 weeks were age- and gender- matched and randomly assigned to each group. For the in vitro assays, samples and cell conditions were randomly distributed across treatment groups.
Blinding	For in vivo experiments, there was no blinding in collection and analysis of the experimental data due to requirements for cage labeling and staffing needs. For in vitro experiments, all the treatments were performed in a parallel manner without the risk of bias in interpretation. All data were acquired and analyzed by softwares with object standard. Therefore, blinding was not relevant to the study.

# Reporting for specific materials, systems and methods

We require information from authors about some types of materials, experimental systems and methods used in many studies. Here, indicate whether each material, system or method listed is relevant to your study. If you are not sure if a list item applies to your research, read the appropriate section before selecting a response.

## Materials & experimental systems

n/a	Involved in the study
<input type="checkbox"/>	<input checked="" type="checkbox"/> Antibodies
<input type="checkbox"/>	<input checked="" type="checkbox"/> Eukaryotic cell lines
<input checked="" type="checkbox"/>	<input type="checkbox"/> Palaeontology and archaeology
<input type="checkbox"/>	<input checked="" type="checkbox"/> Animals and other organisms
<input checked="" type="checkbox"/>	<input type="checkbox"/> Clinical data
<input checked="" type="checkbox"/>	<input type="checkbox"/> Dual use research of concern

## Methods

n/a	Involved in the study
<input checked="" type="checkbox"/>	<input type="checkbox"/> ChIP-seq
<input type="checkbox"/>	<input checked="" type="checkbox"/> Flow cytometry
<input checked="" type="checkbox"/>	<input type="checkbox"/> MRI-based neuroimaging

## Antibodies

### Antibodies used

#### Antibodies for western blot:

Anti-spectrin β II (1:1000, F11, sc-376487, Santa Cruz), Anti-St3gal1 (1:500, LS-C747031, LS Bio), Anti-HER2/ErbB2 (1:500, 2242S, Cell Signaling), Anti-β-Actin (1:5000, 13E5, 4970S, Cell Signaling), Anti-CD18 (1:1000, ab131044, Abcam), Anti-MyH9 (1:500, Poly19098, 909801, Biolegend), Anti-β-Spectrin II (1:1000, 42/B-Spectrin II, 612562, BD biosciences), Anti-α-Spectrin II (1:1000, 35/α-Spectrin II, 612560, BD biosciences), Anti-SPC24 (1:1000, NBP2-47264, Novus Bio), Anti-rabbit IgG, HRP-linked Antibody (1:3000, 7074S, Cell signaling), Anti-mouse IgG, HRP-linked Antibody (1:3000, 7076S, Cell signaling)

#### Antibodies for Immunoprecipitation:

Anti-human CD18 (14 µg/ml, CBR LFA1/2, 366302, Biolegend), Anti-human CD11a (14 µg/ml, TS2/4, Biolegend)

#### Antibodies for flow cytometry:

Anti-mouse CD16/CD32 (1 µg/million cells in 100 µl, 2.4G2, 553142, BD Bioscience), PE anti-human IgG Fc (1 µg/million cells in 100 µl, 12-4998-82, eBioscience), DyLight/650-anti-Human IgG Fc (1 µg/million cells in 100 µl, SA5-10137, Invitrogen), FITC anti-mouse CD45.1 (1 µg/million cells in 100 µl, A20, 110705, Biolegend), BV711 anti-mouse CD45.2 (0.25 µg/million cells in 100 µl, 104, 109847, Biolegend), PE/Cy7 anti-mouse CD8a (0.25 µg/million cells in 100 µl, 53-6.7, 100722, Biolegend), AF594 anti-mouse CD8a (0.25 µg/million cells in 100 µl, 53-6.7, 100758, Biolegend), AF488 anti-mouse CD11a (0.25 µg/million cells in 100 µl, M17/4, 101111, Biolegend), AF647 anti-mouse CD11a (0.25 µg/million cells in 100 µl, M17/4, 101114, Biolegend), BV421 anti-mouse IFN-γ (0.25 µg/million cells in 100 µl, XMG1.2, 505829, Biolegend), BV421 anti-mouse TNF-α (0.25 µg/million cells in 100 µl, MP6-XT22, 506327, Biolegend), BV605 anti-mouse CD366 (Tim-3) (0.5 µg/million cells in 100 µl, RMT3-23, 119721, Biolegend), BV421 anti-mouse CD279 (PD-1) (0.125 µg/million cells in 100 µl, 29F.1A12, 135217, Biolegend), APC anti-mouse Ki-67 (0.25 µg/million cells in 100 µl, 16A8, 652406, Biolegend), Anti-human CD18 (10 µg/ml, CBR LFA1/2, 366302, Biolegend), Anti-human CD11a (10 µg/ml, TS2/4, 350602, Biolegend), AF647 goat anti-mouse IgG (2 µg/ml, Poly4053, 405322, Biolegend), Anti-mouse CD18 (10 µg/ml, M18/2, 101401, Biolegend), AF647 goat anti-rat IgG (2 µg/ml, Poly4053, 405416, Biolegend), APC anti-human/mouse Granzyme B (5 µl/million cells in

100 µl, QA18A28, 396407, Biolegend)

#### Antibodies for Imaging:

AF594 anti-human HER2 (10 µg/ml, 191924, FAB1129T, R&D systems), BV711 anti-mouse CD11c (10 µg/ml, N418, 117349, Biolegend), BV711 anti-mouse I-A/I-E (10 µg/ml, M5/114.15.2, 107643, Biolegend), PB anti-mouse CD31 (5 µg/100 µl, 390, 102422, Biolegend), AF647 anti-mouse CD31 Antibody (5 µg/100 µl, 390, 102415, Biolegend)

#### Antibodies for EM:

anti-LFA-1 (1:100, H155-78, 141002, biologend), biotinylated goat anti-rat IgG (H+L) (1:200, BA-9400-1.5, Vector Lab), ExtrAvidin-Peroxidase (1:150, E2886, Sigma-Aldrich)

#### Antibodies for in vivo experiment:

Anti-mouse CD49d (200 µg/mL, R1-2, 103630, Biolegend), Anti-mouse CD11a (200 µg/mL, M17/4, 101118, Biolegend)

#### Antibodies for mouse T cell culture:

Anti-mouse CD3e (6 µg/mL, 145-2C11, 553057, BD Biosciences), Anti-mouse CD28 (1.6 µg/mL, 37.51, 102102, Biolegend)

#### Antibodies for human T cell culture:

Dynabeads™ Human T-Activator CD3/CD28 (11131D, Thermo Fisher)

## Validation

All reagents are commercially available and have been validated by the respective companies as well as in previously published studies. We also evaluated all the antibodies used in this study for the degree of non-specific binding (as measured in samples that do not express the epitope) or by using isotype controls for comparison.

#### Western blot:

Anti-spectrin β II (1:1000, F11, sc-376487, Santa Cruz): <https://www.scbt.com/p/spectrin-beta-ii-antibody-f-11>  
 Anti-St3gal1 (1:500, LS-C747031, LS Bio): <https://www.lsbio.com/antibodies/st3gal1-antibody-wb-western-ls-c747031/772628>  
 Anti-HER2/ErbB2 (1:500, 2242S, Cell Signaling): <https://www.cellsignal.com/products/primary-antibodies/her2-erbb2-antibody/2242>  
 Anti-β-Actin (1:5000, 13E5, 4970S, Cell Signaling): <https://www.cellsignal.com/products/primary-antibodies/b-actin-13e5-rabbit-mab/4970>  
 Anti-CD18 (1:1000, ab131044, Abcam): <https://www.abcam.com/cd18-antibody-ab131044.html>  
 Anti-MyH9 (1:500, Poly19098, 909801, Biolegend): <https://www.biologend.com/en-us/products/purified-non-muscle-myosin-heavy-chain-ii-a-antibody-11471>  
 Anti-β-Spectrin II (42/B-Spectrin II, 612562, BD biosciences): <https://www.bdbiosciences.com/en-us/products/reagents/microscopy-imaging-reagents/immunofluorescence-reagents/purified-mouse-anti-spectrin-ii.612562>  
 Anti-α-Spectrin II (35/α-Spectrin II, 612560, BD biosciences): <https://www.bdbiosciences.com/en-us/products/reagents/microscopy-imaging-reagents/immunofluorescence-reagents/purified-mouse-anti-spectrin-ii.612560>  
 Anti-SPC24 (1:1000, NBP2-47264, Novus Bio): [https://www.novusbio.com/products/spc24-antibody\\_nbp2-47264](https://www.novusbio.com/products/spc24-antibody_nbp2-47264)  
 gclid=CjwKCAiAoL6eBhA3EiwAXDom5uXMc5LU2-k6VZOFMSIXKC-IAw0-C\_GBJIXJ0AOj38mqKQK9E76mBoC5DAQAvD\_BwE&gclsrc=aw.ds  
 Anti-rabbit IgG, HRP-linked Antibody (1:3000, 7074S, Cell signaling): <https://www.cellsignal.com/products/secondary-antibodies/anti-rabbit-igg-hrp-linked-antibody-7074>  
 Anti-mouse IgG, HRP-linked Antibody (1:3000, 7076S, Cell signaling): <https://www.cellsignal.com/products/secondary-antibodies/anti-mouse-igg-hrp-linked-antibody/7076?N=4294960093+102287+4294956287&fromPage=plp>

#### Immunoprecipitation:

Anti-human CD18 (14 µg/ml, CBR LFA1/2, 366302, Biolegend): <https://www.biologend.com/en-us/products/purified-anti-human-cd18-antibody-10821>  
 Anti-human CD11a (14 µg/ml, TS2/4, 350602, Biolegend): <https://www.biologend.com/en-us/products/purified-anti-human-cd11a-antibody-6971>

#### Flow cytometry:

Anti-mouse CD16/CD32 (1 µg/million cells in 100 µl, 2.4G2, 553142, BD Bioscience): <https://www.bdbiosciences.com/en-ca/products/reagents/flow-cytometry-reagents/research-reagents/single-color-antibodies-ruo/purified-rat-anti-mouse-cd16-cd32-mouse-bd-fc-block.553142>  
 PE anti-human IgG Fc (1 µg/million cells in 100 µl, 12-4998-82, eBioscience): <https://www.thermofisher.com/antibody/product/Goat-anti-Human-IgG-Fc-Secondary-Antibody-Polyclonal/12-4998-82>  
 DyLight/650-anti-Human IgG Fc (1 µg/million cells in 100 µl, SA5-10137, Invitrogen): <https://www.thermofisher.com/antibody/product/Goat-anti-Human-IgG-Fc-Cross-Adsorbed-Secondary-Antibody-Polyclonal/SA5-10137>  
 FITC anti-mouse CD45.1 (1 µg/million cells in 100 µl, A20, 110705, Biolegend): <https://www.biologend.com/en-us/products/fitc-anti-mouse-cd45-1-antibody-198>  
 BV711 anti-mouse CD45.2 (0.25 µg/million cells in 100 µl, 104, 109847, Biolegend): <https://www.biologend.com/en-us/products/brilliant-violet-711-anti-mouse-cd45-2-antibody-13278>  
 PE/Cy7 anti-mouse CD8a (0.25 µg/million cells in 100 µl, 53-6.7, 100722, Biolegend): <https://www.biologend.com/en-us/products/pe-cyanine7-anti-mouse-cd8a-antibody-1906>  
 AF594 anti-mouse CD8a (0.25 µg/million cells in 100 µl, 53-6.7, 100758, Biolegend): <https://www.biologend.com/en-us/products/alex-fluor-594-anti-mouse-cd8a-antibody-9608>  
 PE anti-mouse LFA-1 (0.25 µg/million cells in 100 µl, H155-78, 141005, Biolegend): <https://www.biologend.com/en-us/products/pe-anti-mouse-cd11a-cd18-lfa-1-antibody-7042>  
 AF488 anti-mouse CD11a (0.25 µg/million cells in 100 µl, M17/4, 101111, Biolegned): <https://www.biologend.com/en-us/products/alex-fluor-488-anti-mouse-cd11a-antibody-3200>  
 AF647anti-mouse CD11a (0.25 µg/million cells in 100 µl, M17/4, 101114, Biolegned): <https://www.biologend.com/en-us/products/alex-fluor-647-anti-mouse-cd11a-antibody-3201>  
 BV421 anti-mouse IFN-γ (0.25 µg/million cells in 100 µl, XMG1.2, 505829, Biolegend): <https://www.biologend.com/en-us/products/brilliant-violet-421-anti-mouse-ifn-gamma-antibody-7154>  
 BV421 anti-mouse TNF-α (0.25 µg/million cells in 100 µl, MP6-XT22, 506327, Biolegend): <https://www.biologend.com/en-us/>

products/brilliant-violet-421-anti-mouse-tnf-alpha-antibody-7336  
 BV605 anti-mouse CD366 (Tim-3) (0.5 µg/million cells in 100 µl, RMT3-23, 119721, Biolegend): <https://www.biolegend.com/en-us/products/brilliant-violet-605-anti-mouse-cd366-tim-3-antibody-13391>  
 BV421 anti-mouse CD279 (PD-1) (0.125 µg/million cells in 100 µl, 29F.1A12, 135217, Biolegend): <https://www.biolegend.com/en-us/products/brilliant-violet-421-anti-mouse-cd279-pd-1-antibody-7330>  
 APC anti-mouse Ki-67 (0.25 µg/million cells in 100 µl, 16A8, 652406, Biolegend): <https://www.biolegend.com/en-us/products/apc-anti-mouse-ki-67-antibody-8447>  
 Anti-human CD18 (10 µg/ml, CBR LFA1/2, Biolegend): <https://www.biolegend.com/en-us/products/purified-anti-human-cd18-antibody-10821>  
 Anti-human CD11a (10 µg/ml, TS2/4, Biolegend): <https://www.biolegend.com/en-us/products/purified-anti-human-cd11a-antibody-6971>  
 AF647 goat anti-mouse IgG (2 µg/ml, Poly4053, 405322, Biolegend): <https://www.biolegend.com/en-us/products/alexa-fluor-647-goat-anti-mouse-igg-minimal-x-reactivity-9283>  
 Anti-mouse CD18 (10 µg/ml, M18/2, 101401, Biolegend): <https://www.biolegend.com/en-us/products/purified-anti-mouse-cd18-antibody-361>  
 AF647 goat anti-rat IgG (2 µg/ml, Poly4053, 405416, Biolegend): <https://www.biolegend.com/en-us/products/alexa-fluor-647-goat-anti-rat-igg-minimal-x-reactivity-9252>  
 APC anti-human/mouse Granzyme B (5 µl/million cells in 100 µl, QA18A28, 396407, Biolegend): <https://www.biolegend.com/en-us/products/apc-anti-human-mouse-granzyme-b-recombinant-antibody-17568?GroupID=GROUP28>

Imaging:  
 AF594 anti-human HER2 (10 µg/ml, 191924, FAB1129T, R&D systems): [https://www.rndsystems.com/products/human-erb2-her2-alexa-fluor-594-conjugated-antibody-191924\\_fab1129t](https://www.rndsystems.com/products/human-erb2-her2-alexa-fluor-594-conjugated-antibody-191924_fab1129t)  
 BV711 anti-mouse CD11c (10 µg/ml, N418, 117349, Biolegend): <https://www.biolegend.com/en-us/products/brilliant-violet-711-anti-mouse-cd11c-antibody-10175>  
 BV711 anti-mouse I-A/I-E (10 µg/ml, M5/114.15.2, 107643, Biolegend): <https://www.biolegend.com/en-us/products/brilliant-violet-711-anti-mouse-i-a-i-e-antibody-12086>  
 PB anti-mouse CD31 (5 µg/100 µl, 390, 102422, Biolegend): <https://www.biolegend.com/en-us/products/pacific-blue-anti-mouse-cd31-antibody-6669>  
 AF647 anti-mouse CD31 Antibody (5 µg/100 µl, 390, 102415, Biolegend): <https://www.biolegend.com/en-us/products/alexa-fluor-647-anti-mouse-cd31-antibody-3092>

EM:  
 anti-LFA-1 (1:100, H155-78, 141002, biolegend): <https://www.biolegend.com/en-us/products/purified-anti-mouse-cd11a-cd18-lfa-1-antibody-7040>  
 biotinylated goat anti-rat IgG (H+L) (1:200, BA-9400-1.5, Vector Lab): <https://vectorlabs.com/products/antibodies/biotinylated-goat-anti-rat-igg>  
 ExtrAvidin-Peroxidase (1:150, E2886, Sigma-Aldrich): [https://www.sigmal Aldrich.com/US/en/product/sigma/e2886?gclid=Cj0KCQjAgaGgBhC8ARlsAAAyLfF6YkmW67ENLukGQHtzNpiXtcfodbyv\\_Zzd1xH4uJ9Bl\\_gNFwjAkDsaAsexEALw\\_wcB&gclsrc=aw.ds](https://www.sigmal Aldrich.com/US/en/product/sigma/e2886?gclid=Cj0KCQjAgaGgBhC8ARlsAAAyLfF6YkmW67ENLukGQHtzNpiXtcfodbyv_Zzd1xH4uJ9Bl_gNFwjAkDsaAsexEALw_wcB&gclsrc=aw.ds)

In vivo experiment:  
 Anti-mouse CD49d (200 µg/mL, R1-2, 103630, Biolegend): <https://www.biolegend.com/en-us/products/ultra-leaf-purified-anti-mouse-cd49d-antibody-18975>  
 Anti-mouse CD11a (200 µg/mL, M17/4, 101118, Biolegend): <https://www.biolegend.com/en-us/products/ultra-leaf-purified-anti-mouse-cd11a-antibody-8079>

T cell culture:  
 Anti-mouse CD3e (6 µg/mL, 145-2C11, 553057, BD Biosciences): <https://www.bdbiosciences.com/en-us/products/reagents/flow-cytometry-reagents/research-reagents/single-color-antibodies-ruo/purified-na-le-hamster-anti-mouse-cd3e.553057>  
 Anti-mouse CD28 (1.6 µg/mL, 37.51, 102102, Biolegend): <https://www.biolegend.com/en-us/search-results/purified-anti-mouse-cd28-antibody-117>  
 Dynabeads™ Human T-Activator CD3/CD28 (11131D, Thermo Fisher): [https://www.thermofisher.com/order/catalog/product/11131D?cid=bid\\_sap\\_cdx\\_r01\\_co\\_cp1434\\_pjt8107\\_ext1905\\_0so\\_blg\\_op\\_awa\\_kt\\_s00\\_dynas5](https://www.thermofisher.com/order/catalog/product/11131D?cid=bid_sap_cdx_r01_co_cp1434_pjt8107_ext1905_0so_blg_op_awa_kt_s00_dynas5)

## Eukaryotic cell lines

Policy information about [cell lines and Sex and Gender in Research](#)

Cell line source(s)

B16F10, Phoenix and bEND.3 cells were originally obtained from ATCC.  
 Platinum-E cells were purchased from Cell Biolabs, Inc.  
 B16-OVA and B16-hHER2 cells were generated from B16F10 cells originally obtained from ATCC.

Authentication

The cell lines were not authenticated.

Mycoplasma contamination

The cell lines were not tested for mycoplasma contamination.

Commonly misidentified lines  
 (See [ICLAC](#) register)

No commonly misidentified cell lines were used.

## Animals and other research organisms

Policy information about [studies involving animals](#); [ARRIVE guidelines](#) recommended for reporting animal research, and [Sex and Gender in Research](#)

### Laboratory animals

C57BL/6, OT-I TCR (C57BL/6-Tg(TcrαTcrβ)1100Mjb/J), OT-II TCR (B6.Cg-Tg(TcrαTcrβ)425Cbn/J), LFA-1 KO (B6.129S7-Itgαltm1Bll/J), Cas9 (B6J.129(Cg)-Gt(ROSA)26Sortm1.1(CAG-cas9\*,EGFP)Fezh/J), B6-GFP (C57BL/6-Tg(UBC-GFP)30Scha/J) and ROSA tdTomato (B6.Cg-Gt(ROSA)26Sortm14(CAG-tdTomato)Hze/J) mice were purchased from the Jackson Laboratory (Bar Harbor, ME). CD11a-mYFP, CD18-mCFP, and GFP-ROSA bII-spectrin mice were generated at the Gene Targeting and Transgenic Core facility at the University of Rochester. HER2 transgenic mice were obtained from Genentech. LFA-1 heterozygous mice were generated through breeding LFA-1 KO mice (Jackson) with C57BL/6 mice. Cas9/OT1 mice were generated through breeding Cas9 mice (Jackson) with OT1 mice (Jackson). Six- to 10-week-old female or male mice were used in this study. The mice were maintained under 12-hour light/dark cycles at 22°C and 40 to 50% humidity.

### Wild animals

This study did not involve wild animals.

### Reporting on sex

Sex is not a factor in our data analyses as it is well-known that sex does not significantly affect cytotoxic functions of CD8 T cells.

### Field-collected samples

The study did not involve samples collected from the field.

### Ethics oversight

All animal experiments were performed in the Association for Assessment and Accreditation of Laboratory Animal Care International (AAALAC)-accredited, specific pathogen-free facilities in the Division of Laboratory Animal Resources of the University of Rochester Medical Center (URMC). All animal experiments were approved by the University Committee on Animal Resources at the University of Rochester (Rochester, NY, USA).

Note that full information on the approval of the study protocol must also be provided in the manuscript.

## Flow Cytometry

### Plots

Confirm that:

- The axis labels state the marker and fluorochrome used (e.g. CD4-FITC).
- The axis scales are clearly visible. Include numbers along axes only for bottom left plot of group (a 'group' is an analysis of identical markers).
- All plots are contour plots with outliers or pseudocolor plots.
- A numerical value for number of cells or percentage (with statistics) is provided.

### Methodology

#### Sample preparation

Flow cytometry and cell sorting were performed at the University of Rochester Medical Center (URMC) Flow Core. Sample preparation for each experiment is described in detail in the methods section.

For isolation of lymphocytes from organ tissues and tumors, mice were euthanized, and organs and tumors were extracted. Lungs, livers, and tumors were minced into small fragments and digested with 1 mg/ml collagenase D (Sigma) and 50 mg/ml DNase (Roche) at 37°C for 45 min, passed through a 40 µm cell strainer, and lymphocytes were isolated via Percoll gradient centrifugation. LNs and spleens were made single cells through 70 µm cell strainers. RBCs in single cells suspensions were lysed with ACK lysis buffer (Thermo), washed with DBPS. For in vitro T cells staining, they were re-stimulated with PMA/Ionomycin before staining.

#### Instrument

LSRII 18 color flow cytometer (BD Bioscience)  
FACS Aria (BD Bioscience)

#### Software

FlowJo software (v.10.8)

#### Cell population abundance

The purifies of the sorted sgRNA-transduced T cells or CD8 T cells were more than 95%.

#### Gating strategy

Gating strategy is provided in each figure legend and the Method section. Briefly, based on the pattern of FSC-A/SSC-A, cells in the lymphocytes gate were used for analysis for T cell subsets. Singlets were gated according to the pattern of FSC-H/FSC-A. Positive populations were selected by the specific antibodies. For the sorting of sgRNA transduced Cas9/OT1 T cells, we included RFP+GFP+ population. For the sorting of CAR-T cells from lungs, we included GFP+ population.

- Tick this box to confirm that a figure exemplifying the gating strategy is provided in the Supplementary Information.